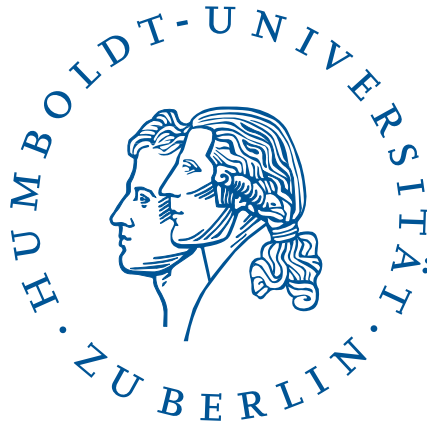


Ab-initio calculation of Raman spectra of
graphene-based materials

MASTERARBEIT

zur Erlangung des akademischen Grades
Master of Science
(M. Sc.)
im Fach Physik



eingereicht an der
Mathematisch-Naturwissenschaftlichen Fakultät I
Institut für Physik
Humboldt-Universität zu Berlin

von
Herr Albin Hertrich
geboren am 23.09.1987 in Starnberg

Gutachter:

1. *Prof. Dr. Dr. h.c. Claudia Draxl*
2. *Prof. Dr. Jürgen P. Rabe*

Betreuung:

1. *Dr. Caterina Cocchi*
2. *PD Dr. Pasquale Pavone*
3. *Prof. Dr. Dr. h.c. Claudia Draxl*

eingereicht am: 25. Juli 2016

Contents

Introduction	1
1 Raman scattering in graphene-based materials	2
2 Raman scattering in crystals	5
2.1 The Raman effect	5
2.2 The Raman-scattering efficiency	5
2.3 Raman efficiency and dielectric tensor	7
3 Theoretical background and methodology	9
3.1 Adiabatic approximation	9
3.2 Vibrations in the harmonic approximation	10
3.3 Density-functional theory	12
3.4 Optical properties	13
3.4.1 Time-dependent density-functional theory	13
3.4.2 Bethe-Salpeter equation	14
4 Implementation	16
4.1 The exciting code	16
4.1.1 The (L)APW(+lo) basis	16
4.1.2 Phonons in the supercell approach	17
4.2 Raman scattering	19
4.2.1 Derivatives of the dielectric function	19
4.2.2 Vibrational matrix elements	20
4.2.3 Interpolation over the Brillouin zone	21
5 Graphene-based materials: structural, electronic, dielectric, and phonon properties	22
5.1 Structure optimization	22
5.2 Kohn-Sham band structure	23
5.3 Dielectric function	24
5.4 Phonons	25
6 First-order Raman spectra: The G-band	27
6.1 Graphene	27
6.1.1 Dielectric function of displaced structures	27
6.1.2 Raman spectra	29
6.1.3 Resonance behavior	29
6.2 Other graphene-based materials	30

7	Second-order Raman spectra: The 2D-band	31
7.1	Graphene	31
7.1.1	Dielectric function of displaced structures	32
7.1.2	Raman spectrum	35
7.2	AA graphite	35
7.3	AB bilayer graphene	36
7.4	AB graphite	38
7.5	Effect of layer stacking	40
8	Conclusions and outlook	41
A	Two dimensional materials	49
B	Convergence with respect to numerical parameters	50
B.1	Phonons frequencies	50

Introduction

The unique electronic and mechanical properties have been keeping graphene in the focus of research for more than a decade. As a lightweight, transparent, and flexible conductor, graphene is a promising candidate for a wide range of applications. For the characterization of graphene-based materials, Raman spectroscopy has become the standard tool. The topic of this thesis is the calculations of first- and second-order Raman spectra of graphene-based materials from first principles.

A Raman scattering experiment is an optical probe, which gives access to both optical and vibrational properties. For calculating Raman scattering intensities, we need to obtain vibrational and optical properties. The former is calculated by frozen-phonon calculations. The latter can be treated on different levels of theory, from the independent-particle level up to a full many-body treatment by solving the Bethe-Salpeter equation. Our approach for calculating Raman scattering intensities is based on the dependence of the macroscopic dielectric function on the phonon normal coordinates. Two ingredients enter the calculation of Raman scattering intensities: Vibrational matrix elements and derivatives of the dielectric function. Both can be calculated independently once the phonon normal coordinates are known. Calculations are done fully *ab-initio* with the full-potential all-electron density-functional-theory package **exciting** [10], which implements all the methods mentioned above.

During the course of this thesis, second-order Raman scattering was implemented in **exciting**. The implementation is specifically tuned to materials, with resonant contributions to the second-order Raman spectrum. Instead of calculating the full spectrum, only the resonant parts are included. The broad non-resonant part, which often resembles the phonon overtone density of states, is not included in this implementation. To reduce the numerical complexity, we restrict the calculations of second-order Raman spectra to overtones of the transverse optical in-plane phonons along the Γ -K path of the Brillouin zone. The implementation is applied to the family of graphene-based materials to calculate first- and second-order Raman spectra. The effect of both the stacking sequence and the excitation energy on the spectra is explored.

This thesis is structured as follows: Chapter 1 introduces the graphene-based materials under investigation. In Chapter 2, the approach for calculating Raman scattering intensities is derived. Chapter 3 gives a theoretical background of the computational methods, while Chapter 4 presents the implementation of Raman scattering in the **exciting** code. In Chapter 5, results for the structural, electronic, optical, and vibrational properties of graphene-based materials are shown. The main results, the first- and second-order Raman spectra of these materials, are presented in Chapters 6 and 7. Finally, in Chapter 8, conclusions and an outlook for further studies are given.

Chapter 1

Raman scattering in graphene-based materials

Graphene-based materials are interesting from both the experimental and theoretical point of view. While the electronic properties of graphene were already predicted in 1946 by Wallace [52], the production of freestanding monolayer graphene stayed a challenging task for more than half a century. Only in 2004 Novoselov and Geim [27] found a way to produce nearly charge-neutral monolayers of graphene, by depositing graphene layers, which they had extracted from bulk graphite, on a SiO surface. From that point on graphene production methods evolved rapidly (see, *e.g.*, Refs. [30] and [29]). In the following, a brief description of the materials, which are going to be studied here, is given.

Graphene is a two-dimensional crystal, made of carbon atoms, which form a hexagonal honeycomb-lattice with point group symmetry $6/mmm$ in Hermann-Mauguin notation, or D_{6h} in Schönflies notation. The lattice vectors of the rhombical primitive unit cell (Fig. 1.1) can be chosen as

$$\mathbf{a}_1 = a \left(\frac{1}{2}, \frac{\sqrt{3}}{2} \right) \quad (1.1)$$

$$\mathbf{a}_2 = a \left(-\frac{1}{2}, \frac{\sqrt{3}}{2} \right), \quad (1.2)$$

with lattice constant a . The unit cell contains two atoms, located at $(0,0)$ and $(\frac{1}{3}, \frac{1}{3})$, given in lattice coordinates. The reciprocal lattice vectors are given by

$$\mathbf{b}_1 = \frac{2\pi}{a} \left(1, \frac{\sqrt{3}}{2} \right) \quad (1.3)$$

$$\mathbf{b}_2 = \frac{2\pi}{a} \left(-1, \frac{\sqrt{3}}{2} \right). \quad (1.4)$$

The Brillouin zone (BZ) is a hexagon. The irreducible BZ is the triangle confined by the Γ -K-M- Γ path (see Fig. 1.1).

Bulk graphite consists of an infinite number graphene layers, weakly bound via van der Waals interaction. The simplest way in which the layers can be aligned relative to each other, is the AA, or simple hexagonal, stacking, where each atom of a layer is situated directly on top of an atom of the neighboring layer. AA stacked

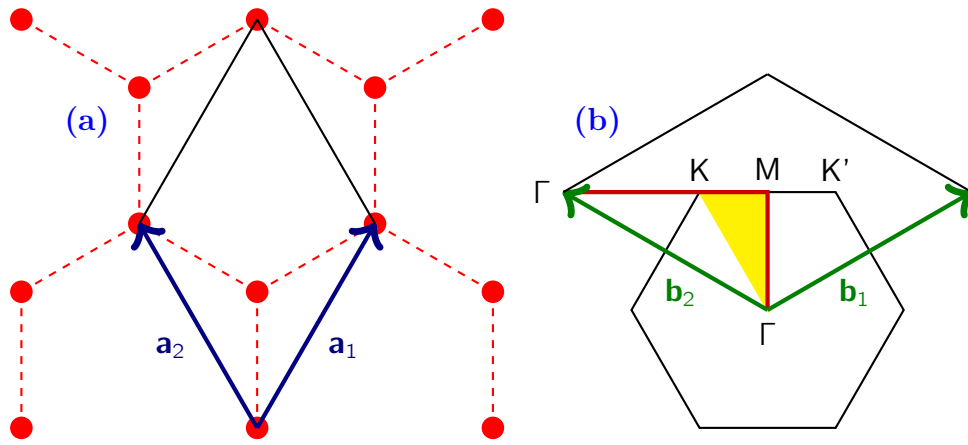


Figure 1.1: (a) Unit cell of graphene with lattice vectors \mathbf{a}_1 and \mathbf{a}_2 . (b) Reciprocal-space unit cell with reciprocal lattice vectors \mathbf{b}_1 and \mathbf{b}_2 . The hexagon represents the first BZ, with the yellow area being the irreducible part. The path along the high-symmetry points Γ , K, and M is marked in red.

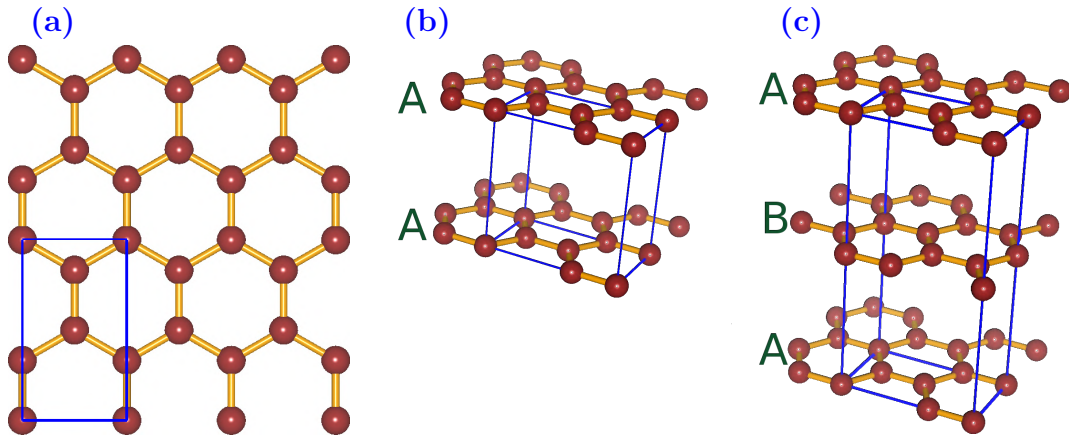


Figure 1.2: Stacking of graphene sheets: (a) graphene sheet, (b) AA stacking, (c) AB stacking.

graphite has, however, not been observed yet. Previous *ab-initio* studies [2][44] have shown, that while from a thermodynamic point of view AA graphite could exist, it is mechanically unstable, due to a negative shear modulus. Still, AA graphite is an interesting model system to investigate the effect of the stacking arrangement on the Raman signals. It has a small unit cell, containing only two atoms, and is periodic in all three directions.

AB, or Bernal, graphite is the most stable configuration. Every second layer is shifted so that there is an atom on top of each carbon ring of the neighboring layers (see Fig. 1.2). At ambient conditions, a typical sample of bulk crystalline graphite consists mainly of AB graphite. Usually, also a certain amount of rhombohedral (ABC) stacked graphite is contained, where the third layer is shifted against both the first and the second layer [21]. This configuration is, however, not considered here.

Detailed information from an experimental point of view on the application of Raman spectroscopy on graphene-based materials can be found in the review paper

by Ferrari and Basko [8] and references therein. The Raman spectrum of pristine graphene shows two strong peaks: the first-order G-band at $\approx 1580 \text{ cm}^{-1}$ and the second-order 2D-band at $\approx 2700 \text{ cm}^{-1}$. Additionally, there are two weak second-order peaks that are usually labeled as 2D' and D+D''. Raman spectra of defected graphene additionally contain various other peaks of comparable intensity. Typical Raman spectra of pristine and defected graphene, is shown in Fig. 1.3.

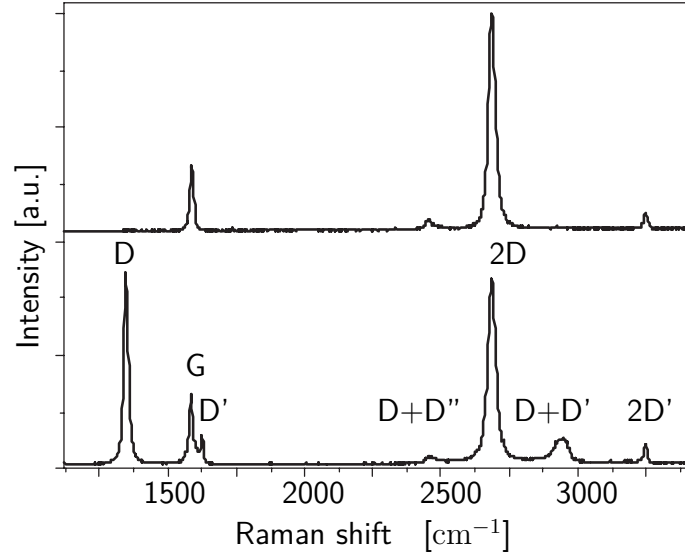


Figure 1.3: Experimental Raman spectrum of pristine (top) and defected (bottom) graphene from Ref. [8].

From Raman spectra of graphene-based materials, a lot of information can be extracted. Information about the number of layers in a polylayer graphene sample is typically extracted from the 2D-band. The G-band is sensitive to the doping level, while the defect concentration can be determined from the intensity of the peaks, specific to defected graphene.

Chapter 2

Raman scattering in crystals

In this chapter, the method to calculate first-order and second-order overtone Raman spectra is introduced. A systematic derivation of the approach used to calculate Raman-scattering efficiencies can be found in Ref. [16]. A more general overview over Raman scattering is given in many textbooks, or for example in Refs. [22], [12], and [4].

2.1 The Raman effect

The Raman effect is based on inelastic scattering of photons. Predicted in 1923 by Smekal [45], it was first experimentally observed and reported in 1928 independently by Raman and Krishnan [37] in liquids, and by Landsberg and Mandelstam [18] in quartz crystals. In solids, the difference in energy between the absorbed and emitted photon usually comes from the creation or annihilation of one or more phonons. Processes with one phonon involved are called first-order processes, while second-order processes involve two phonons. The first qualitative theoretical description of the first- and second-order Raman effect was given by Fermi and Rasetti in 1931 [6]. The scattered photons can either be lower (Stokes scattering), or higher (anti-Stokes scattering) in energy, as visualized in Fig. 2.1. In this thesis, only intensities of Stokes processes are calculated.

2.2 The Raman-scattering efficiency

The Raman-scattering efficiency is defined as

$$S = \frac{1}{V_s} \frac{d\sigma}{d\Omega}, \quad (2.1)$$

where V_s is the scattering volume and $\frac{d\sigma}{d\Omega}$ is the differential scattering cross-section.

There are two different approaches widely used in the literature to determine Raman-scattering efficiencies. In a first approach, the Raman process is separated into, at least, three individual scattering processes:

- production of an electron-hole pair from an absorbed photon;
- one or more electron-phonon or hole-phonon scattering processes;
- recombination of the electron and hole via the emission of a photon.

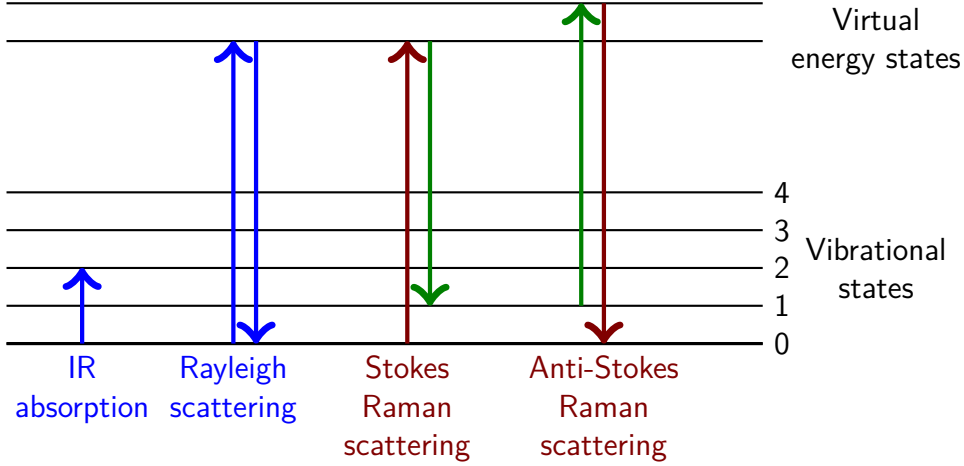


Figure 2.1: Different processes of interaction between matter and light. In a infrared process, a photon is absorbed and a phonon with the same energy is created without emission of a photon. In Rayleigh processes an electron-hole pair is created and recombined; the scattered photon is not shifted in energy. In (anti-) Stokes Raman processes the scattered photon energy is reduced (increased) through the creation (annihilation) of a phonon.

Each process is treated by first-order in perturbation theory. The scattering cross-section is determined by Fermi's golden rule. The resonant contribution to the scattering efficiency for a first-order Raman process with initial state i and final state f is given by

$$S_{i \rightarrow f} \propto \left| \sum_{AB} \frac{M_{fB} M_{BA} M_{Ai}}{(\epsilon_i - \epsilon_B - i\gamma_B/2)(\epsilon_i - \epsilon_A - i\gamma_A/2)} \right|^2 \delta(\epsilon_i - \epsilon_f). \quad (2.2)$$

Here the summation is performed over all virtual intermediate states A and B. ϵ_j is the energy of state j and M_{jk} is the scattering matrix element between states j and k . All states are combined electronic-vibrational states. A similar expression with three intermediate steps is obtained for both second-order processes and defect-induced first-order processes [51]. This approach was recently successfully applied in the second order to monolayer graphene [51], strained monolayer graphene [36], and bilayer graphene [14][35]. When applied to graphene-based materials in the second order, this approach is usually called double-resonant (DR) Raman scattering in the literature, as introduced by Thomsen and Reich [47]. In a recent paper [13], the generality of DR is questioned, because of the additional orders in perturbation theory introduced by electron- or hole-phonon scattering events.

In this thesis, a second approach [16][1] is used, which is described in detail in the next section. This approach makes use of semi-classical radiation theory. The scattering efficiency is obtained directly from the dependence of the macroscopic dielectric function on the atomic coordinates. The use of the dielectric function allows for a treatment on different levels of theory. Fast calculations are possible on the independent-particle level by using time-dependent density-functional theory (TDDFT) in the random phase approximation. Excitonic effects can be included by diagonalizing the full Bethe-Salpeter Hamiltonian. While not so important in the case of graphene-based materials, it was shown that excitonic effects play an important role in the resonance behavior of the first-order Raman spectrum of silicon [9].

2.3 Raman efficiency and dielectric tensor

The connection between the Raman-scattering efficiency introduced in the previous section and the macroscopic dielectric tensor $\varepsilon_{\omega}^{kk'}$ is established by investigating the electric field, which is emitted by an induced dipole. The derivation closely follows Ref. [16].

The dipole-moment per volume V induced by an external electric field with polarization \mathbf{e}_L , intensity E_L , and frequency ω_L is given by

$$\frac{p^k(t)}{V} = \frac{1}{4\pi} E_L(t) \left[\varepsilon_{\omega_L}^{kk'}(t) - \delta^{kk'} \right] e_L^{k'}. \quad (2.3)$$

This dipole, in turn, produces an electric field. The intensity of the scattered field with polarization \mathbf{e}_s at long distance R is given by

$$E_s \left(t + \frac{R}{c} \right) = \frac{1}{c^2 R} \mathbf{e}_s \cdot \ddot{\mathbf{p}}(t), \quad (2.4)$$

where c is the speed of light. Taking the ω_s Fourier coefficient, we obtain for the field scattered in the coherence volume of a phonon, which consists of N_{cell} unit cells with volume V_E :

$$E_s(\omega_s) = \frac{N_{\text{cell}} V_E \omega_s^2}{4\pi c^2 R} \left[E_L e_s^k \varepsilon_{\omega_L}^{kk'} e_L^{k'} \right]_{\omega_s}. \quad (2.5)$$

The scattering power per solid angle, $\frac{dP}{d\Omega}$, is obtained from the time average of the scattered electric field (indicated by the angle brackets):

$$\begin{aligned} \frac{dP}{d\Omega} &= \frac{c}{4\pi} \frac{V_s}{N_{\text{cell}} V_E} \langle E_s, E_s^* \rangle_{\omega_s} R^2 \\ &= \frac{N_{\text{cell}} V_E V_s \omega_s^4}{(4\pi)^3 c^3} \left\langle E_L e_s^k \varepsilon_{\omega_L}^{kk'} e_L^{k'}, E_L^* e_s^{k'*} \varepsilon_{\omega_L}^{kk'*} e_L^{k'} \right\rangle_{\omega_s}. \end{aligned} \quad (2.6)$$

The enhancement factor $V_s/N_{\text{cell}} V_E$ is due to the assumption, that the scattering volume V_s consists of several phonon coherence volumes, which contribute incoherently. The scattering power, in turn, is related to the scattering cross-section by

$$\frac{dP_s}{d\Omega} = \frac{d\sigma}{d\Omega} \frac{\omega_s}{\omega_L} I_L, \quad (2.7)$$

with the excitation energy

$$I_L = \frac{c}{4\pi} \left\langle E_L e_L^{k'}, E_L^* e_L^{k'*} \right\rangle. \quad (2.8)$$

Inserting Eqs. (2.6) and (2.7) in Eq. (2.1), we obtain for the Raman-scattering efficiency in tensor notation

$$S_{\omega_s}^{kk'} = \frac{N_{\text{cell}} V_E \omega_L \omega_s^3}{(4\pi)^2 c^4} \left\langle \delta\varepsilon^{kk'}, \delta\varepsilon^{kk'*} \right\rangle_{\omega_s}. \quad (2.9)$$

The time-average of the fluctuations of the dielectric function, caused by a transition between between initial state $|i\rangle$ and final state $|f\rangle$ is given by the corresponding transition matrix element

$$\left\langle \delta\varepsilon^{kk'}, \delta\varepsilon^{kk'*} \right\rangle_{\omega_s} = \left| \left\langle f \left| \varepsilon_{\omega_L}^{kk'} \right| i \right\rangle_{\omega_s = \omega_L - \omega_{if}} \right|^2. \quad (2.10)$$

The dielectric tensor is a function of the atomic coordinates. As the fluctuations occur due to phonons, we use an expansion of the dielectric function with respect to the phonon normal coordinates $Q_{\mathbf{q}}^j$, which will be discussed explicitly in the next chapter:

$$\epsilon_{\omega_L}^{kk'}(Q) = \epsilon_{\omega_L}^{kk'} \Big|_{Q=0} + \sum_{j\mathbf{q}} \frac{\partial \epsilon_{\omega_L}^{kk'}}{\partial Q_{\mathbf{q}}^j} \Big|_{Q=0} Q_{\mathbf{q}}^j + \sum_{jj'\mathbf{q}\mathbf{q}'} \frac{\partial^2 \epsilon_{\omega_L}^{kk'}}{\partial Q_{\mathbf{q}}^j \partial Q_{\mathbf{q}'}^{j'}} \Big|_{Q=0} Q_{\mathbf{q}}^j Q_{\mathbf{q}'}^{j'} + \mathcal{O}(Q^3). \quad (2.11)$$

Here Q stands for the set of all $Q_{\mathbf{q}}^j$. Within the adiabatic approximation the initial and final state are a product of the electronic and vibrational states $|i\rangle = |g\mu\rangle$. The derivatives of the dielectric function at zero displacement depend only on the electronic states, while the phonon normal coordinates depend only on the vibrational states. Before the absorption and after the emission of the photon, the system is in the electronic ground state, the transition takes place in the vibrational state only.

In the optical limit, the momentum of the photon is negligible. Because of momentum conservation, the sum of all created phonons has to be zero. Inserting the expansion, given in Eq. (2.11), into the expression for the fluctuations of the dielectric function, we obtain

$$\langle f | \epsilon_{\omega_L}^{kk'} | i \rangle_{\omega_s = \omega_L - \omega_{if}} = [\epsilon_{\mu \rightarrow \nu}^{kk'}]_{\omega_s}^{(1)} + [\epsilon_{\mu \rightarrow \nu}^{kk'}]_{\omega_s}^{(2)} + \mathcal{O}(Q^3), \quad (2.12)$$

with the first- and second-order contributions

$$[\epsilon_{\mu \rightarrow \nu}^{kk'}]_{\omega_s}^{(1)} = \sum_j \frac{\partial \epsilon_{\omega_L}^{kk'}}{\partial Q_0^j} \Big|_{Q=0} \langle \nu | Q_0^j | \mu \rangle \quad (2.13)$$

$$[\epsilon_{\mu \rightarrow \nu}^{kk'}]_{\omega_s}^{(2)} = \sum_{jj'\mathbf{q}} \frac{\partial^2 \epsilon_{\omega_L}^{kk'}}{\partial Q_{\mathbf{q}}^j \partial Q_{-\mathbf{q}}^{j'}} \Big|_{Q=0} \langle \nu | Q_{\mathbf{q}}^j Q_{-\mathbf{q}}^{j'} | \mu \rangle. \quad (2.14)$$

The two ingredients of the fluctuations of the dielectric function, derivatives of the dielectric function and phonon matrix elements can be obtained individually, as will be described in Section 4.2. While due to momentum conservation, in first-order processes only Γ -point phonons contribute, the second-order spectrum is generally made up by contributions of any two phonons with opposite momenta within the full first BZ. For the full Raman-scattering efficiency, a summation over all final vibrational states has to be taken. Including thermal occupation of the initial vibrational state, the full Raman-scattering intensity is given by

$$S_{\omega_s}^{kk'} = \frac{N V_E \omega_L \omega_s^3 \sum_{\mu} e^{-E_{\mu}/k_B T} \sum_{\nu} \left| \sum_n [\epsilon_{\mu \rightarrow \nu}^{kk'}]_{\omega_s}^{(n)} \right|^2}{(4\pi)^2 c^4 \sum_{\mu} e^{-E_{\mu}/k_B T}}. \quad (2.15)$$

The expression given in Eq. (2.15) corresponds to the integrated intensity of the Raman line. For a Raman spectrum, which can be directly compared to experiment, a Lorentzian broadening is applied to the Raman-scattering efficiency.

Chapter 3

Theoretical background and methodology

This chapter provides a summary of the theoretical basics, which are necessary to pursue our approach for calculating Raman-scattering intensities. Furthermore, the methods are introduced, which are used to calculate the necessary quantities. Within the adiabatic approximation (Section 3.1) the electronic and nuclear degrees of freedom decouple. Phonon properties are considered within the harmonic approximation (Section 3.2). The electronic problem is solved using density-functional theory (DFT) (Section 3.3). The macroscopic dielectric function can be calculated either from time-dependent DFT, or using many-body perturbation theory by solving the Bethe-Salpeter equation (Section 3.4).

3.1 Adiabatic approximation

The stationary Schrödinger equation of a crystal consisting of electrons and nuclei is given by

$$H(x, X) \Psi(x, X) = E \Psi(x, X) , \quad (3.1)$$

with the Hamiltonian

$$H(x, X) = T_{\text{nuc}}(X) + T_{\text{el}}(x) + U_{\text{nuc-nuc}}(X) + U_{\text{el-el}}(x) + U_{\text{el-nuc}}(x, X) . \quad (3.2)$$

Here, X represents the set of all nuclear coordinates, while x represents the set of all electronic coordinates. The Hamiltonian in Eq. (3.2) consists of kinetic-energy terms (T) and Coulomb terms (U). Indices stand for electronic (el) and nuclear contributions (nuc).

Within the adiabatic approximation the electrons are assumed to follow the motion of the nuclei adiabatically, due to the large ratio (typically $> 10^3$) between mass of the nuclei and electrons. Under this assumption, the electronic and vibrational degrees of freedom can be decoupled. The complete wave function can be written as a product of an electronic wave function $\psi(x; X)$, which depends parametrically on the nuclear coordinates, and a nuclear wave function $\chi(X)$:

$$\Psi(x, X) = \psi(x; X) \chi(X) , \quad (3.3)$$

where $\psi(x; X)$ and $\chi(X)$ fulfill the equations

$$[T_{\text{el}}(x) + U_{\text{el-el}}(x) + U_{\text{el-nuc}}(x; X)] \psi(x; X) = E_{\text{el}}(X) \psi(x; X) , \quad (3.4)$$

$$[T_{\text{nuc}}(X) + V_{\text{ad}}(X)] \chi(X) = E \chi(X) . \quad (3.5)$$

Note, that the electronic energy $E_{\text{el}}(X)$ enters the Schrödinger equation of the nuclei as part of the adiabatic potential

$$V_{\text{ad}}(X) = U_{\text{nuc-nuc}}(X) + E_{\text{el}}(X) . \quad (3.6)$$

3.2 Vibrations in the harmonic approximation

The coordinate $X_l^{\alpha k}$ of an atom α in a unit cell l along the Cartesian direction k is the sum of the lattice vector R_l^k , the equilibrium position in the unit cell $\tau^{\alpha k}$, and the displacement out of equilibrium $u_l^{\alpha k}$:

$$X_l^{\alpha k} = R_l^k + \tau^{\alpha k} + u_l^{\alpha k} . \quad (3.7)$$

Let us assume that the electronic problem is solved, and consider the motion of the atoms in the adiabatic potential given in Eq. (3.6). If displacements are small, the adiabatic potential can be approximated by its expansion with respect to the atomic displacements up to the second order (harmonic approximation):

$$V_{\text{ad}}(u) \approx V_{\text{ad}}(u=0) + \sum_{l\mu} \Phi_l^\mu u_l^\mu + \frac{1}{2} \sum_{l'l''\mu\mu'} \Phi_{l'l''}^{\mu\mu'} u_l^\mu u_{l''}^{\mu'} . \quad (3.8)$$

Here the Cartesian index α and the atomic index k are combined to the index $\mu = \{k, \alpha\}$, and u represents the set of all u_l^μ . The first-order coefficients in Eq. (3.8), Φ_l^μ , are the negative forces acting on the atoms at zero displacement:

$$\Phi_l^\mu = \left. \frac{\partial V_{\text{ad}}}{\partial u_l^\mu} \right|_{u=0} = -F_l^\mu(u=0) . \quad (3.9)$$

As forces on the atoms at equilibrium are zero, the first-order coefficients are all vanishing. The second-order coefficients, $\Phi_{l'l''}^{\mu\mu'}$, are the harmonic interatomic force constants, that can be written as negative derivatives of the forces:

$$\Phi_{l'l''}^{\mu\mu'} = \left. \frac{\partial^2 V_{\text{ad}}}{\partial u_l^\mu \partial u_{l''}^{\mu'}} \right|_{u=0} = - \left. \frac{\partial F_l^\mu}{\partial u_{l''}^{\mu'}} \right|_{u=0} . \quad (3.10)$$

The force constants form a $3 N_{\text{cell}} N_{\text{at}}$ dimensional matrix Φ , where N_{cell} is the number of unit cells in the phonon coherence volume and N_{at} is the number of atoms in each unit cell. From the definition given in Eq. (3.10), it follows that the force-constant matrix is symmetric. As the total energy is minimal at equilibrium, the matrix Φ is positive definite. Furthermore, for all Cartesian directions α the sum of the force constants of all atomic sites is zero

$$\sum_{lk} \Phi_{l'l''}^{\mu\mu'} = 0 , \quad (3.11)$$

as this corresponds to the energy change due to a translation of the whole crystal. From translational symmetry, it is obvious that the force constants cannot depend

on the individual lattice vectors \mathbf{R}_l and $\mathbf{R}_{l'}$, but only on the distance $\mathbf{R}_{l''} = \mathbf{R}_{l'} - \mathbf{R}_l$, which again is a lattice vector, labeled by l'' :

$$\Phi_{l''}^{\mu\mu'} = \Phi_{0,l''}^{\mu\mu'} . \quad (3.12)$$

Finally, for many systems, the number of independent force constants can be further reduced, making use of the crystal symmetry.

Within the harmonic approximation, the Hamiltonian of the nuclei given in Eq. (3.5) is reduced to

$$H_{\text{nuc}} = T_{\text{nuc}} + V_{\text{ad}}(0) + \frac{1}{2} \sum_{l''\mu\mu'} \Phi_{l''}^{\mu\mu'} u_l^\mu u_{l'}^{\mu'} , \quad (3.13)$$

which describes a system of $3 N_{\text{cell}} N_{\text{at}}$ coupled harmonic oscillators. With the definition of the dynamical matrix in reciprocal space

$$D_{\mathbf{q}}^{\mu\mu'} = \frac{1}{\sqrt{M_k M_{k'}}} \sum_{l'} \Phi_{0,l'}^{\mu\mu'} e^{i\mathbf{q}\cdot\mathbf{R}_{l'}} , \quad (3.14)$$

the problem is further reduced to solving N_{cell} systems of $3 N_{\text{at}}$ coupled oscillators. Diagonalization of the dynamical matrix

$$\sum_{\mu'} D_{\mathbf{q}}^{\mu\mu'} w_{\mathbf{q}}^{j\mu'} = (\omega_{\mathbf{q}}^j)^2 w_{\mathbf{q}}^{j\mu} , \quad (3.15)$$

leads to the phonon frequencies $\omega_{\mathbf{q}}^j$ and orthonormal eigenvectors $w_{\mathbf{q}}^{j\mu}$ of phonon mode $j = 1, \dots, 3 N_{\text{at}}$. The eigenvectors can be chosen to fulfill the condition

$$w_{-\mathbf{q}}^{j\mu} = (w_{\mathbf{q}}^{j\mu})^* . \quad (3.16)$$

The atomic displacements associated to a phonon eigenmode j at wave-vector \mathbf{q} are defined as:

$$u_l^\mu(Q_{\mathbf{q}}^j) = \frac{1}{\sqrt{N_{\text{cell}} M_\mu}} w_{\mathbf{q}}^{j\mu} e^{i\mathbf{q}\cdot\mathbf{R}_l} Q_{\mathbf{q}}^j , \quad (3.17)$$

where $Q_{\mathbf{q}}^j$ is the complex phonon normal coordinate. For actually displacing atoms in a crystal, it is useful to define real phonon displacement patterns

$$\begin{aligned} \bar{u}_l^\mu(\bar{Q}_{\mathbf{q}}^j) &= \frac{1}{2\sqrt{N_{\text{cell}} M_\mu}} \left(w_{\mathbf{q}}^{j\mu} e^{i\mathbf{q}\cdot\mathbf{R}_l} + w_{-\mathbf{q}}^{j\mu} e^{-i\mathbf{q}\cdot\mathbf{R}_l} \right) \bar{Q}_{\mathbf{q}}^j \\ &= \frac{1}{\sqrt{N_{\text{cell}} M_\mu}} \Re \left(w_{\mathbf{q}}^{j\mu} e^{i\mathbf{q}\cdot\mathbf{R}_l} \right) \bar{Q}_{\mathbf{q}}^j \end{aligned} \quad (3.18)$$

with real normal coordinates $\bar{Q}_{\mathbf{q}}^j$. In a similar way, it is also possible to construct real displacements from the imaginary part of Eq. (3.17).

3.3 Density-functional theory

For the knowledge of the adiabatic potential $V_{\text{ad}}(X) = U_{\text{nuc-nuc}}(X) + E_{\text{el}}(X)$, the electronic problem has to be solved in order to obtain the ground-state energy of the electronic system for a given nuclear configuration. Hence, we have to face the problem of N interacting electrons, which, in the adiabatic approximation, has $3N$ degrees of freedom. Solving the many-body Schrödinger equation given in Eq. (3.5) is only possible for small systems. Instead, density-functional theory (DFT) is used. DFT is based on the Hohenberg-Kohn theorem [15], which states that every ground-state property of a many-electron system is a unique functional of the ground-state electron density $n(\mathbf{r})$. In other words, the explicit knowledge of the full many-body wave function is not necessary. In particular, this holds for the ground-state total energy

$$E[n] = T_0[n] + E_{\text{H}}[n] + E_{\text{XC}}[n] + E_{\text{ext}}[n] , \quad (3.19)$$

and its contributions: the non-interacting kinetic energy $T_0[n]$, the electrostatic Hartree energy $E_{\text{H}}[n]$, the exchange-correlation (XC) energy $E_{\text{XC}}[n]$, and the external energy $E_{\text{ext}}[n]$. In practice, only the functional dependence of the Hartree energy

$$E_{\text{H}}[n] = \frac{1}{2} \int d^3r \int d^3r' \frac{n(\mathbf{r})n(\mathbf{r}')}{|\mathbf{r} - \mathbf{r}'|} = \frac{1}{2} \int d^3r v_{\text{H}}(\mathbf{r}) n(\mathbf{r}) , \quad (3.20)$$

with the Hartree potential $v_{\text{H}}(\mathbf{r})$, and the contributions from the external potential $v_{\text{ext}}(\mathbf{r})$

$$E_{\text{ext}}[n] = \int d^3r v_{\text{ext}}(\mathbf{r}) n(\mathbf{r}) \quad (3.21)$$

are known analytically. The total energy must be minimized to find the ground-state electron density. For the explicit minimization of Eq. (3.19), a fictitious system of non-interacting electrons, called Kohn-Sham (KS) system, is introduced. The orthonormal KS wave functions $\varphi_i(\mathbf{r})$ lead to the electron density of the real system

$$n(\mathbf{r}) = \sum_{i=1}^N |\varphi_i(\mathbf{r})|^2 . \quad (3.22)$$

Using the variational theorem to minimize the total energy with respect to the KS wave functions leads to the KS equation [17]

$$\left[-\frac{1}{2} \nabla^2 + v_{\text{KS}}(\mathbf{r}) \right] \varphi_i(\mathbf{r}) = \epsilon_i \varphi_i(\mathbf{r}) \quad (3.23)$$

with the KS potential

$$v_{\text{KS}}(\mathbf{r}) = v_{\text{H}}(\mathbf{r}) + v_{\text{XC}}(\mathbf{r}) + v_{\text{ext}}(\mathbf{r}) , \quad (3.24)$$

where the XC potential is the functional derivative of the XC energy with respect to the electron density

$$v_{\text{XC}}(\mathbf{r}) = \frac{\delta E_{\text{XC}}}{\delta n(\mathbf{r})} . \quad (3.25)$$

As the KS potential is a functional of the electron density, the KS equation has to be solved in a self-consistent way. The XC energy functional includes all exchange and correlation effects. As no exact expression for the XC energy is known, it has

to be approximated. The simplest approximation is the local density approximation (LDA)

$$E_{XC}^{\text{LDA}} = \int d^3r \varepsilon_{XC}^h(n(\mathbf{r})) n(\mathbf{r}) , \quad (3.26)$$

where $\varepsilon_{XC}^h(\rho)$ is the XC energy per electron of a homogeneous electron gas with density ρ . While the exchange part is known analytically, the correlation part usually uses parameters fitted to Monte Carlo data, which fulfills the known exact behavior in the limit of low and high density. A step beyond LDA is the generalized gradient approximation (GGA), where the XC energy also depends on the electron-density gradient [19]. A commonly used GGA is the XC functional parameterized by Perdew, Burke, and Ernzerhof (PBE) [31]. Finally, there are more sophisticated functionals going beyond semi-local DFT, which are not described here.

3.4 Optical properties

The calculation of the macroscopic dielectric function requires the treatment of electronic excitations, for which it is necessary to go beyond ground-state DFT. This is possible either by applying time-dependent DFT, or using many-body perturbation theory, by solving the Bethe-Salpeter equation.

3.4.1 Time-dependent density-functional theory

Time-dependent (TD) DFT is the generalization of DFT to the time domain. On the basis of the Runge-Gross theorem [41], which is the TD counterpart of the Hohenberg-Kohn theorem, a set of TD KS equations can be derived. The TD effective KS-potential is given by

$$v_{\text{KS}}(\mathbf{r}, t) = v_{\text{ext}}(\mathbf{r}, t) + v_{\text{H}}(\mathbf{r}, t) + v_{\text{XC}}(\mathbf{r}, t) . \quad (3.27)$$

All exchange and correlation effects are included in the TD XC-potential $v_{\text{XC}}(\mathbf{r}, t)$, which depends on the electron density of the system of all previous times.

Instead of solving the TD KS equation, a perturbative approach in the linear response regime can be used [33] for obtaining the dielectric tensor. The key quantity here is the XC-kernel, which is defined as the functional derivative of the TD XC-potential with respect to the TD electron density

$$f_{\text{XC}}(\mathbf{r}, \mathbf{r}', t - t') = \frac{\delta v_{\text{XC}}(\mathbf{r}, t)}{\delta n(\mathbf{r}', t')} . \quad (3.28)$$

The starting point is the KS response function, which is given in Fourier space in the basis of reciprocal lattice vectors by

$$\chi_{\mathbf{G}\mathbf{G}'}^0(\mathbf{q}, \omega) = \frac{1}{N_{\mathbf{k}} V_E} \sum_{nm\mathbf{k}} \frac{f_{n\mathbf{k}} - f_{m\mathbf{k}+\mathbf{q}}}{\varepsilon_{n\mathbf{k}} - \varepsilon_{m\mathbf{k}+\mathbf{q}} + \omega + i\eta} M_{nm\mathbf{k}}(\mathbf{q}, \mathbf{G}) M_{nm\mathbf{k}}^*(\mathbf{q}, \mathbf{G}') . \quad (3.29)$$

Here $f_{n\mathbf{k}}$ is the Fermi-Dirac distribution. The matrix elements are given by

$$M_{nm\mathbf{k}}(\mathbf{q}, \mathbf{G}) = \frac{\sqrt{4\pi}}{|\mathbf{q} + \mathbf{G}|} \langle n\mathbf{k} | e^{i(\mathbf{q}+\mathbf{G})\cdot\mathbf{r}} | m\mathbf{k} + \mathbf{q} \rangle , \quad (3.30)$$

with

$$M_{nm\mathbf{k}}(\mathbf{q} \rightarrow 0, 0) = \sqrt{4\pi} \frac{\langle n \mathbf{k} | \hat{\mathbf{p}}_{nm} | m \mathbf{k} \rangle}{\epsilon_{n\mathbf{k}} - \epsilon_{m\mathbf{k}}} . \quad (3.31)$$

The reducible interacting density-response function

$$\chi(\mathbf{r}, \mathbf{r}', t - t') = \frac{\delta n(\mathbf{r}, t)}{\delta v_{\text{ext}}(\mathbf{r}', t')} \quad (3.32)$$

is connected to χ^0 via the XC kernel by a Dyson-equation

$$\chi(\mathbf{q}, \omega) = \chi^0(\mathbf{q}, \omega) + \chi^0(\mathbf{q}, \omega) [f_{\text{H}}(\mathbf{q}) + f_{\text{XC}}(\mathbf{q}, \omega)] \chi(\mathbf{q}, \omega) , \quad (3.33)$$

where f_{H} is the Coulomb kernel. From the density-response function, the inverse microscopic dielectric function is obtained by

$$\varepsilon^{-1}(\mathbf{q}, \omega) = 1 + f_{\text{H}} \chi(\mathbf{q}, \omega), \quad (3.34)$$

which in return is related to the macroscopic dielectric function by

$$\varepsilon_{\text{M}}(\mathbf{q}, \omega) = \frac{1}{\varepsilon_{00}^{-1}(\mathbf{q}, \omega)} . \quad (3.35)$$

Like the XC functional in DFT, f_{XC} has to be approximated. Several local and non-local approximations exist [28][39][40]. A rather crude approximation is the random phase approximation (RPA)

$$f_{\text{XC}}^{\text{RPA}} = 0, \quad (3.36)$$

in which excitonic effects are not captured at all. Nevertheless electronic excitations in metals are usually well described in RPA, due to the strong screening in metals.

3.4.2 Bethe-Salpeter equation

When excitonic effects play a role, an explicit many-body treatment is achieved by solving the Bethe-Salpeter equation (BSE) of many-body perturbation theory [43][11][46] that treats neutral excitations. An important role for the calculation of optical properties plays the two-particle correlation function, which is given in terms of one and two particle Green's functions by

$$S(\mathbf{r}_1, \mathbf{r}_2, \mathbf{r}_3, \mathbf{r}_4, \omega) = -G_2(\mathbf{r}_1, \mathbf{r}_2, \mathbf{r}_3, \mathbf{r}_4, \omega) + G(\mathbf{r}_1, \mathbf{r}_3, \omega) G(\mathbf{r}_2, \mathbf{r}_4, \omega) . \quad (3.37)$$

The correlation function is connected to the density-response function defined in Eq. (3.32) by contraction of indices:

$$\chi(\mathbf{r}, \mathbf{r}', \omega) = -i S(\mathbf{r}, \mathbf{r}, \mathbf{r}', \mathbf{r}', \omega) . \quad (3.38)$$

The BSE is a Dyson equation for the correlation function

$$S = S_0 + S_0 K S , \quad (3.39)$$

where S_0 is the non-interacting correlation function and K the electron-hole pair interaction kernel. In the particle-hole basis, the BSE can be mapped to a linear algebra problem, by the introduction of the BSE Hamiltonian in matrix form

$$\mathbf{H}^{\text{eff}} = \mathbf{H}^{\text{diag}} + 2 \mathbf{H}^{\text{x}} + \mathbf{H}^{\text{c}} . \quad (3.40)$$

The diagonal part of the Hamiltonian

$$H_{v\mathbf{k},v'\mathbf{k}'}^{\text{diag}} = (\epsilon_{c\mathbf{k}} - \epsilon_{v\mathbf{k}}) \delta_{v,v'} \delta_{c,c'} \delta_{\mathbf{k},\mathbf{k}'} \quad (3.41)$$

describes independent particle (IP) transitions between valence states, labeled v , and conduction states, labeled c . The repulsive exchange term

$$H_{v\mathbf{k},v'\mathbf{k}'}^{\text{x}} = \int d^3r d^3r' \varphi_{v\mathbf{k}}(\mathbf{r}) \varphi_{c\mathbf{k}}^*(\mathbf{r}) \bar{v}_C(\mathbf{r}, \mathbf{r}') \varphi_{v'\mathbf{k}'}^*(\mathbf{r}') \varphi_{c'\mathbf{k}'}(\mathbf{r}') \quad (3.42)$$

originates from the unscreened short-ranged Coulomb interaction, given by $\bar{v}_C(\mathbf{r}, \mathbf{r}')$. The attractive direct term is given by

$$H_{v\mathbf{k},v'\mathbf{k}'}^{\text{c}} = - \int d^3r d^3r' \varphi_{v\mathbf{k}}(\mathbf{r}) \varphi_{c\mathbf{k}}^*(\mathbf{r}') W(\mathbf{r}, \mathbf{r}') \varphi_{v'\mathbf{k}'}^*(\mathbf{r}) \varphi_{c'\mathbf{k}'}(\mathbf{r}') , \quad (3.43)$$

with the screened Coulomb potential in reciprocal space

$$W_{\mathbf{G}\mathbf{G}'}(\mathbf{q}) = [\delta_{\mathbf{G}\mathbf{G}'} - \chi_{\mathbf{G}\mathbf{G}'}^0(\mathbf{q}, 0)] v_{\mathbf{G}'}(\mathbf{q}) , \quad (3.44)$$

where $\chi_{\mathbf{G}\mathbf{G}'}^0$ is the IP response function, that is normally approximated by the KS response function defined in Eq. (3.29).

After diagonalization of the BSE Hamiltonian

$$\mathbf{H}^{\text{eff}} \cdot \mathbf{A}^\lambda = E^\lambda \mathbf{A}^\lambda , \quad (3.45)$$

the correlation function can be written in spectral representation in terms of the eigenvalues E^λ and eigenvectors $A_{v\mathbf{k}}^\lambda$:

$$S_{v\mathbf{k},v'\mathbf{k}'} = i \sum_\lambda \frac{A_{v\mathbf{k}}^\lambda A_{v'\mathbf{k}'}^{\lambda*}}{\omega - E^\lambda} . \quad (3.46)$$

Using Eq. (3.34) and (3.35), the macroscopic dielectric tensor is given by

$$\epsilon_M^{\alpha\beta}(\omega) = 1 - \frac{8\pi^2}{N_{\mathbf{k}} V_E} \sum_\lambda |t_\lambda^\alpha t_\lambda^{\beta*}| \left[\frac{1}{\omega - E^\lambda + i\eta} + \frac{1}{-\omega - E^\lambda - i\eta} \right] , \quad (3.47)$$

with

$$t_\lambda^\alpha = \frac{\langle v\mathbf{k} | \hat{p}_\alpha | c\mathbf{k} \rangle}{\epsilon_{c\mathbf{k}} - \epsilon_{v\mathbf{k}}} . \quad (3.48)$$

Chapter 4

Implementation

In this chapter, the implementation of Raman scattering in the **exciting** code is described. Section 4.1 introduces **exciting**, with a special focus on the basis set and on the supercell method for calculating phonon properties. In Section 4.2, it is explained how the first- and second-order Raman-scattering intensities are calculated.

4.1 The **exciting** code

The **exciting** code [10] is a full-potential all-electron DFT package. It applies linearized augmented plane waves and local orbitals as basis functions, which are presented in the next subsection. It allows for the calculation of various ground-state properties, as well as phonon properties in the supercell approach. **exciting** has a special focus on excited state properties, which are treated in the framework of TDDFT or many-body perturbation theory [42].

4.1.1 The (L)APW(+lo) basis

When solving the KS equation (3.23) numerically, an appropriate basis is required. Close to the nuclei, the KS wave functions present strong oscillations, while between the atoms they are smooth and vary slowly. This motivates the use of augmented plane wave (APW). In this case, the unit cell is divided into atomic spheres, also called muffin-tins spheres (MT) with radii R_{MT}^α , and an interstitial region (I). Within the I , the basis-functions are described by plane wave, while within the MTs, they are augmented by atomic-like functions:

$$\phi_{\mathbf{k}+\mathbf{G}}(\mathbf{r}) = \begin{cases} \sum_{lm} A_{lm\alpha}^{\mathbf{k}+\mathbf{G}} u_{l\alpha}(r_\alpha) Y_{lm}(\hat{\mathbf{r}}_\alpha) & r_\alpha \leq R_{\text{MT}}^\alpha \\ \frac{1}{\sqrt{V}} e^{i(\mathbf{k}+\mathbf{G})\mathbf{r}} & \mathbf{r} \in I \end{cases}, \quad (4.1)$$

with the coordinate

$$\mathbf{r}_\alpha = \mathbf{r} - \mathbf{R}_\alpha = r_\alpha \hat{\mathbf{r}}_\alpha \quad (4.2)$$

in the MT around atom α , centered at \mathbf{R}_α . V is the crystal volume, Y_{lm} are spherical harmonics with angular momentum quantum numbers l and m , and the radial functions $u_{l\alpha}$ are solutions of the radial Schrödinger equation with spherically averaged potential within the MT. The coefficients $A_{lm\alpha}^{\mathbf{k}+\mathbf{G}}$ are determined by the continuous condition at the MT boundary.

As the radial functions are energy-dependent, the KS equations in the APW basis-functions are non-linear in energy. There are several ways to get rid of the energy dependence, as described for example in Refs. [10] and [23]. One way is to use the linearized APW (LAPW) basis, in which the APWs are linearized around fixed energy values.

$$\phi_{\mathbf{k}+\mathbf{G}}^{\text{MT}}(\mathbf{r}) = \sum_{lm} \left[A_{lm\alpha}^{\mathbf{k}+\mathbf{G}} u_{l\alpha}(r_\alpha; \epsilon_{l\alpha}) + B_{lm\alpha}^{\mathbf{k}+\mathbf{G}} \dot{u}_{l\alpha}(r_\alpha; \epsilon_{l\alpha}) \right] Y_{lm}(\hat{\mathbf{r}}_\alpha), \quad (4.3)$$

with the energy derivative of the radial function

$$\dot{u}_{l\alpha}(r_\alpha; \epsilon) = \frac{\partial u(r_\alpha; \epsilon)}{\partial \epsilon}. \quad (4.4)$$

The coefficients $A_{lm\alpha}^{\mathbf{k}+\mathbf{G}}$ and $B_{lm\alpha}^{\mathbf{k}+\mathbf{G}}$ are determined to fulfill smoothness of the basis functions at the MT boundary.

A second way is to use APWs with fixed energy parameters in combination with local orbitals (APW+lo), which are strictly zero everywhere, except in one MT, where they are defined as

$$\phi_\mu^{\text{lo}}(\mathbf{r}) = [a_\mu u_\mu(r_\mu; \epsilon_\mu) + b_\mu \dot{u}_\mu(r_\mu; \epsilon_\mu)] Y_\mu(\hat{\mathbf{r}}_\mu). \quad (4.5)$$

Here μ is a combination of the indices l , m , and α .

In **exciting** [10], the (L)APW(+lo) basis family is used, a combination of LAPW and APW+lo. Additional local orbitals can be added to the basis, which may contain radial functions at additional energy parameters, or higher derivatives of radial functions. The KS equation is mapped to a generalized eigenvalue-problem

$$\mathbf{H}^{\mathbf{k}} \cdot \mathbf{C}^{\mathbf{k}} = \epsilon^{\mathbf{k}} \mathbf{S}^{\mathbf{k}} \cdot \mathbf{C}^{\mathbf{k}}, \quad (4.6)$$

with the Hamiltonian matrix $\mathbf{H}^{\mathbf{k}}$ and the overlap matrix $\mathbf{S}^{\mathbf{k}}$.

4.1.2 Phonons in the supercell approach

A simple way to obtain the interatomic force constants and dynamical matrix introduced in the previous section is the *frozen-phonon approximation*, in which force constants are obtained from forces acting on the atoms, when applying small displacements to the atoms.

Let's first have a look again at the definition of the dynamical matrix given in Eq. (3.14). Using Eq. (3.12), we can write

$$\begin{aligned} D_{\mathbf{q}}^{\mu\mu'} &= \frac{1}{\sqrt{M_k M_{k'}}} \sum_{l'} \Phi_{0,l'}^{\mu\mu'} e^{i\mathbf{q} \cdot \mathbf{R}_{l'}} \\ &= \frac{1}{N_{\text{SC}}} \frac{1}{\sqrt{M_k M_{k'}}} \sum_{l'} \sum_{l \in \text{SC}} \Phi_{ll'}^{\mu\mu'} e^{i\mathbf{q} \cdot \mathbf{R}_{l'}}, \end{aligned} \quad (4.7)$$

where l'' fulfills the condition $\mathbf{R}_{l''} = \mathbf{R}_l + \mathbf{R}_{l'}$. SC is a supercell containing N_{SC} unit cells, which corresponds to a vibration with wavevector \mathbf{q} . The second sum includes all l , which belong to lattice vectors $\mathbf{R}_l \in \text{SC}$. Replacing the sum over l' by a sum over l'' , we obtain

$$D_{\mathbf{q}}^{\mu\mu'} = \frac{1}{N_{\text{SC}}} \frac{1}{\sqrt{M_k M_{k'}}} \sum_{l''} \sum_{l \in \text{SC}} \Phi_{ll''}^{\mu\mu'} e^{i\mathbf{q} \cdot (\mathbf{R}_{l''} - \mathbf{R}_l)}. \quad (4.8)$$

In the supercell, the periodic real displacements $u_l^\nu(\Delta, c, \mu)$ and $u_l^\nu(\Delta, s, \mu)$ are applied, where

$$u_l^\nu(\Delta, c, \mu) = \delta_{\nu\mu} \Delta \cos(\mathbf{q} \cdot \mathbf{R}_l) , \quad (4.9)$$

$$u_l^\nu(\Delta, s, \mu) = \delta_{\nu\mu} \Delta \sin(\mathbf{q} \cdot \mathbf{R}_l) . \quad (4.10)$$

In both cases, the atom α is displaced in the Cartesian direction k , specified by the combined index μ . All other atoms in the supercell stay in the equilibrium position. Cosine-like displacements represent the real part, while sine-like displacements represent the imaginary part of a complex displacement pattern. Using Eq. (3.10), we can write

$$\begin{aligned} \sum_{\nu'} \Phi_{l\nu'}^{\mu\mu'} e^{i\mathbf{q} \cdot \mathbf{R}_l} &= \sum_{\nu'} -\frac{\partial F_l^\mu}{\partial u_{\nu'}^\mu} (\cos \mathbf{q} \cdot \mathbf{R}_l + i \sin \mathbf{q} \cdot \mathbf{R}_l) . \\ &\approx -\frac{F_l^\mu(u(2\Delta, c, \mu')) - F_l^\mu(u(\Delta, c, \mu'))}{\Delta} \\ &\quad - i \frac{F_l^\mu(u(2\Delta, s, \mu')) - F_l^\mu(u(\Delta, s, \mu'))}{\Delta} . \end{aligned} \quad (4.11)$$

Here, the derivative of the forces with respect to the atomic displacement is approximated by a finite difference of forces. The indices l and ν in the displacements u are omitted for the sake of simplicity. A dynamical matrix element is then given as a sum of contributions of all unit cells in the supercell with the corresponding phase factor:

$$\begin{aligned} D_{\mathbf{q}}^{\mu\mu'} &= \frac{1}{N_{\text{SC}}} \frac{1}{\sqrt{M_k M_{k'}}} \sum_{l \in \text{SC}} e^{-i\mathbf{q} \cdot \mathbf{R}_l} \sum_{\nu'} \Phi_{l\nu'}^{\mu\mu'} e^{i\mathbf{q} \cdot \mathbf{R}_{l'}} \\ &\approx \frac{1}{N_{\text{SC}}} \frac{1}{\sqrt{M_k M_{k'}}} \sum_{l \in \text{SC}} e^{-i\mathbf{q} \cdot \mathbf{R}_l} \left[-\frac{F_l^\mu(u(2\Delta, c, \mu')) - F_l^\mu(u(\Delta, c, \mu'))}{\Delta} \right. \\ &\quad \left. - i \frac{F_l^\mu(u(2\Delta, s, \mu')) - F_l^\mu(u(\Delta, s, \mu'))}{\Delta} \right] . \end{aligned} \quad (4.12)$$

For the calculation of the full dynamical matrix at one \mathbf{q} -point, each atom of the unit cell has to be displaced twice in each Cartesian direction applying both sine- and cosine-like displacements, which leads to a total number of $12 N_{\text{at}}$ calculations.

Using this supercell approach, the direct calculation of the dynamical matrix at arbitrary \mathbf{q} can be computationally very demanding (*e.g.*, for very small $|\mathbf{q}|$, very large supercells have to be considered). Instead one commonly uses an alternative approach, in which first the dynamical matrix is calculated on a grid of $\bar{\mathbf{q}}$ -vectors and Fourier-transformed to real-space to obtain the mass-weighted force constant matrix:

$$D_l^{\mu\mu'} = \frac{1}{N_{\bar{\mathbf{q}}}} \sum_{n=1}^{N_{\bar{\mathbf{q}}}} D_{\bar{\mathbf{q}}_n}^{\mu\mu'} e^{-i\bar{\mathbf{q}}_n \cdot \mathbf{R}_l} . \quad (4.13)$$

The dynamical matrix at arbitrary \mathbf{q} is obtained by Fourier interpolation

$$D_{\mathbf{q}}^{\mu\mu'} = \sum_l D_l^{\mu\mu'} e^{i\mathbf{q} \cdot \mathbf{R}_l} . \quad (4.14)$$

In this approach, for a good description of phonon properties the convergence with respect to the density of the chosen $\bar{\mathbf{q}}$ points is essential.

4.2 Raman scattering

Raman scattering intensities are calculated in **exciting** by evaluating Eq. (2.15). We need to calculate two ingredients: Vibrational matrix elements and derivatives of the dielectric function. Within this thesis, a version of second-order Raman scattering has been implemented on the basis of an already existing first-order implementation. The existing code had to be extended to deal with supercells, to make it possible to apply phonon displacements with finite wavevector. Furthermore, a method for the interpolation of the second derivatives of the dielectric function over the BZ, which is suitable for graphene-based materials had to be found and implemented.

4.2.1 Derivatives of the dielectric function

For calculating Raman-scattering efficiencies, it is necessary to compute derivatives of the macroscopic dielectric function with respect to the phonon normal coordinates. This is done in the *frozen-phonon approximation*, where the displacements of the atoms are treated as a quasi-static perturbation. We use the real displacement patterns defined in Eq. (3.18). All derivatives are evaluated at equilibrium. For the sake of simplicity, the subscript $Q = 0$ is omitted here.

For the connection between derivatives with respect to real and complex normal coordinates, we first have a look at the derivatives of a general observable \mathcal{A} . As for Γ -point phonons the phonon eigenvectors can be chosen real, all derivatives of any observable \mathcal{A} with respect to the real and complex normal coordinates are equal:

$$\frac{\partial^i \mathcal{A}}{\partial Q_0^{j^i}} = \frac{\partial^i \mathcal{A}}{\partial \bar{Q}_0^{j^i}}. \quad (4.15)$$

For an arbitrary \mathbf{q} , using the chain rule, the first derivative of \mathcal{A} with respect to the phonon normal coordinates, expressed in terms of derivatives with respect to atomic displacements is given by

$$\frac{\partial \mathcal{A}}{\partial Q_{\mathbf{q}}^j} = \sum_{l\mu} \frac{\partial \mathcal{A}}{\partial u_l^\mu} \frac{\partial u_l^\mu}{\partial Q_{\mathbf{q}}^j} = \sum_{l\mu} \frac{\partial \mathcal{A}}{\partial u_l^\mu} \frac{1}{\sqrt{N_{\text{cell}} M_\mu}} w_{\mathbf{q}}^{j\mu} e^{i\mathbf{q}\cdot\mathbf{R}_l}. \quad (4.16)$$

The derivatives with respect to the real normal coordinates fulfill the conditions:

$$\begin{aligned} \frac{\partial \mathcal{A}}{\partial \bar{Q}_{\mathbf{q}}^j} &= \sum_{l\mu} \frac{\partial \mathcal{A}}{\partial u_l^\mu} \frac{1}{2\sqrt{N_{\text{cell}} M_\mu}} \left[w_{\mathbf{q}}^{j\mu} e^{i\mathbf{q}\cdot\mathbf{R}_l} + w_{-\mathbf{q}}^{j\mu} e^{-i\mathbf{q}\cdot\mathbf{R}_l} \right] \\ &= \frac{1}{2} \left[\frac{\partial \mathcal{A}}{\partial Q_{\mathbf{q}}^j} + \frac{\partial \mathcal{A}}{\partial Q_{-\mathbf{q}}^j} \right] \end{aligned} \quad (4.17)$$

$$\begin{aligned} \frac{\partial^2 \mathcal{A}}{\partial \bar{Q}_{\mathbf{q}}^{j^2}} &= \sum_{l\mu\mu'} \frac{\partial^2 \mathcal{A}}{\partial u_l^\mu \partial u_{l'}^{\mu'}} \frac{1}{4 N_{\text{cell}} \sqrt{M_\mu M_{\mu'}}} \left[w_{\mathbf{q}}^{j\mu} e^{i\mathbf{q}\cdot\mathbf{R}_l} + w_{-\mathbf{q}}^{j\mu} e^{-i\mathbf{q}\cdot\mathbf{R}_l} \right] \\ &\quad \times \left[w_{\mathbf{q}}^{j\mu'} e^{i\mathbf{q}\cdot\mathbf{R}_{l'}} + w_{-\mathbf{q}}^{j\mu'} e^{-i\mathbf{q}\cdot\mathbf{R}_{l'}} \right] \\ &= \frac{1}{4} \left[\frac{\partial^2 \mathcal{A}}{\partial Q_{\mathbf{q}}^{j^2}} + \frac{\partial^2 \mathcal{A}}{\partial Q_{-\mathbf{q}}^{j^2}} + 2 \frac{\partial^2 \mathcal{A}}{\partial Q_{\mathbf{q}}^j \partial Q_{-\mathbf{q}}^j} \right]. \end{aligned} \quad (4.18)$$

To obtain the derivatives of the dielectric function with respect to the real normal coordinates, we calculate the dielectric function for displaced structures and use a polynomial fit:

$$\varepsilon = \varepsilon^{(0)} + \varepsilon_{\mathbf{q}}^{j(1)} \bar{Q}_{\mathbf{q}}^j + \varepsilon_{\mathbf{q}}^{j(2)} \bar{Q}_{\mathbf{q}}^{j^2} + \dots . \quad (4.19)$$

Using Eq. (4.16), for first-order processes the first derivative of the dielectric function is directly given by the first-order coefficient

$$\frac{\partial \varepsilon}{\partial Q_0^j} = \varepsilon_0^{j(1)} . \quad (4.20)$$

Using Eq. (4.17), the second-order coefficient is:

$$\varepsilon_{\mathbf{q}}^{j(2)} = \frac{1}{2} \frac{\partial^2 \varepsilon}{\partial \bar{Q}_{\mathbf{q}}^{j^2}} = \frac{1}{8} \left[\frac{\partial^2 \varepsilon}{\partial Q_{\mathbf{q}}^{j^2}} + \frac{\partial^2 \varepsilon}{\partial Q_{-\mathbf{q}}^{j^2}} \right] + \frac{1}{4} \frac{\partial^2 \varepsilon}{\partial Q_{\mathbf{q}}^j \partial Q_{-\mathbf{q}}^j} . \quad (4.21)$$

For phonons with finite wavevector, the first two terms in Eq. (4.21) belong to processes with momentum transfer. As within the optical limit, the corresponding scattering processes are not allowed, these terms vanish. The second derivative with respect to normal coordinates of phonons with momentum \mathbf{q} and $-\mathbf{q}$ of the same phonon band j is directly given by the second-order coefficient

$$\frac{\partial^2 \varepsilon}{\partial Q_{\mathbf{q}}^j \partial Q_{-\mathbf{q}}^j} = 4 \varepsilon_{\mathbf{q}}^{j(2)} . \quad (4.22)$$

Thus, when calculating the overtone spectrum without contributions from different phonon bands in one process, the one-dimensional fit of the dielectric function given by Eq. (4.19) is sufficient.

4.2.2 Vibrational matrix elements

Within the harmonic approximation the vibrational matrix elements defined in Eqs. (2.13) and (2.14) can be calculated analytically. For simplicity, let us consider for the moment only one phonon mode, with frequency ω and occupation number ν in vibrational state $|\nu\rangle$. The phonon normal coordinate, written in terms of creation- and annihilation-operators (a^\dagger and a), is given by

$$Q = \frac{1}{\sqrt{2\omega}} (a + a^\dagger) . \quad (4.23)$$

Inserting Eq. (4.23) into the first-order phonon matrix elements given in Eq. (2.13), we obtain

$$\begin{aligned} \langle \nu | Q | \mu \rangle &= \frac{1}{\sqrt{2\omega}} \langle \nu | a + a^\dagger | \mu \rangle \\ &= \frac{1}{\sqrt{2\omega}} \left[\sqrt{\mu} \delta_{\nu, \mu-1} + \sqrt{\mu+1} \delta_{\nu, \mu+1} \right] . \end{aligned} \quad (4.24)$$

Here, the first term belongs to an anti-Stokes process, while the second one belongs to a Stokes process. Using the thermal occupation number

$$\bar{n}_{\mathbf{q}}^j = \frac{1}{e^{-\omega_{\mathbf{q}}^j/k_B T} - 1} , \quad (4.25)$$

we obtain from Eq. (2.15)

$$S_{\omega_s}^{\alpha\beta(1)} = \frac{N V_E \omega_L \omega_s^3}{(4\pi)^2 c^4} \sum_j \frac{1}{2 \omega_0^j} \left| \varepsilon_0^{j(1)} \right|^2 (\bar{n}_0^j + 1) \delta(\omega_L - \omega_s - \omega_0^j) \quad (4.26)$$

for the first-order Stokes Raman spectrum within the harmonic approximation.

Note that by using a polynomial fit for the total energy (or the scalar product of forces and eigenvectors), in analogy to Eq. (4.19), it is possible to go beyond the harmonic approximation, and include anharmonic effects. In this case, the first-order matrix elements given in Eq. (4.24) have to be evaluated numerically. This enables transitions forbidden in the harmonic approximation and leads to a first-order Raman spectrum, which includes overtones of the Γ point phonons. In crystals, due to the large coherence volume of the phonons, these anharmonic effects usually play only a minor role in Raman scattering.

Likewise, the harmonic second-order overtone spectrum is given by

$$S_{\omega_s}^{\alpha\beta(2)} = \frac{N V_E \omega_L \omega_s^3}{(4\pi)^2 c^4} \sum_{\mathbf{q}j} \frac{1}{(2 \omega_{\mathbf{q}}^j)^2} \left| 2 \varepsilon_{\mathbf{q}}^{j(2)} \right|^2 (\bar{n}_{\mathbf{q}}^j + 1)^2 \delta(\omega_L - \omega_s - 2 \omega_{\mathbf{q}}^j). \quad (4.27)$$

Here the relation $\omega_{\mathbf{q}}^j = \omega_{-\mathbf{q}}^j$ was used.

4.2.3 Interpolation over the Brillouin zone

For a full calculation of the second-order (overtone) Raman spectrum, an interpolation over the Brillouin zone is necessary. The straightforward way to do so would be to calculate the second derivatives of the dielectric function on a coarse grid and, for each excitation energy, use Fourier interpolation to obtain the derivatives on a dense grid. This method works well for materials where the second derivatives are only varying slowly. In contrast, in graphene-based materials the second-derivatives with respect to the transverse optical phonon modes are resonant at certain excitation energies, depending on the phonon momenta. Using this kind of interpolation will not give the correct resonance-behavior.

To overcome this problem, a way of interpolation, tailored to this specific use case, is used. To each resonance of the second derivative of the dielectric function, a Gaussian is fitted. Instead of interpolating the derivatives for each excitation energy, the width, position, and intensity of the Gaussians is interpolated. Assuming that width, position, and intensity vary slowly, the main features of the derivatives of the dielectric function can be captured between the calculated points with much better accuracy. In combination with the Fourier-interpolated phonon frequencies, the contributions to the resonant second-order Raman spectrum can be calculated. In this theses, only the contributions from phonons along the Γ -K path in the Brillouin zone are considered.

Chapter 5

Graphene-based materials: structural, electronic, dielectric, and phonon properties

In this chapter, we present our results for the electronic, dielectric, and vibrational properties of monolayer graphene, AB bilayer graphene, AA graphite, and AB graphite. All calculations are carried out starting from the equilibrium geometry, which was obtained in a structure optimization. For graphene, the LDA parametrized by Perdew and Wang [32] and the PBE GGA [31] XC functionals are used. For the other materials, only LDA is used, as PBE fails to give an interlayer distance close to the experimental value.

5.1 Structure optimization

The structure optimization is done keeping the full symmetry of the hexagonal lattice. In the case of monolayer graphene, the in-plane lattice constant a is the only degree of freedom. The optimal lattice constant is determined in a fit of the Birch-Murnaghan equation of state to the electronic ground-state energy of structures with different lattice constants. For the three-dimensional hexagonal lattice, additionally the optimal out-of-plane lattice constant c has to be determined. For graphite, a method of alternating the optimization of the volume and the c/a ratio is applied, until a convergence of 1 mÅ is reached. For bilayer graphene, the relaxed interlayer distance of graphite is used. The optimized lattice parameters are given in Table 5.1.

	graphene		graphite		
Stacking			AA	AB	AB
XC-functional	PBE	LDA	LDA	LDA	expt.
In-plane C-C distance [Å]	1.424	1.412	1.412	1.412	1.422
In-plane lattice constant [Å]	2.467	2.445	2.445	2.445	2.464
Interlayer distance [Å]			3.632	3.324	3.356

Table 5.1: Equilibrium lattice parameters for the systems under investigation. Experimental values are taken from Ref. [50].

5.2 Kohn-Sham band structure

The electronic properties of graphene are characterized by π bands, which cross the Fermi energy at the K point exhibiting linear dispersion in its vicinity (see Fig. 5.1a). This makes graphene a zero-gap semiconductor, also called semi-metal. As a consequence of the linear dispersion, the electrons close to the Fermi level behave like massless fermions. They can be formally described by a Dirac equation with effective speed of light given by the Fermi velocity $v_F \approx 10^6 \text{ m s}^{-1} \approx 0.003 c$ [5]. Because of this, the K point is often called Dirac point. Applying GW corrections to the DFT band structure leads to a renormalization of the Fermi velocity by 17%, and the appearance of a kink in the band dispersion near K [48]. The KS band structure of graphene, AA graphite, AB bilayer graphene, and AB graphite is shown in Fig. 5.1.

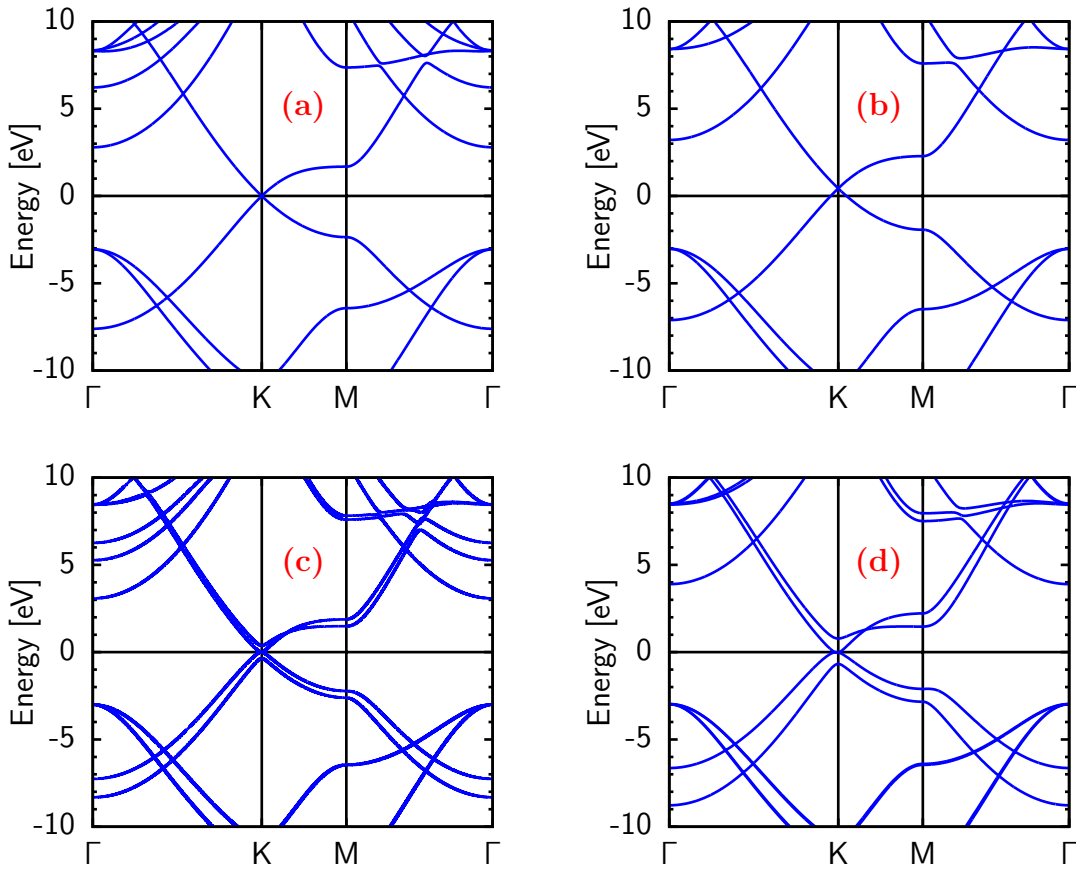


Figure 5.1: KS band structure of (a) monolayer graphene, (b) AA graphite, (c) bilayer graphene, and (d) AB graphite.

In contrast to graphene, AA graphite is a metal. The band crossing at the K point is shifted to positive energies (Fig. 5.1b), giving it a non-zero density of states at the Fermi level. In bilayer graphene (Fig. 5.1c) and AB graphite (Fig. 5.1d), the π bands are parabolic at the K point. Furthermore, there is an additional set of π bands not crossing the Fermi level. Still both materials show semi-metallic behavior with vanishing density of states at the Fermi level.

5.3 Dielectric function

The macroscopic dielectric function is a key ingredient for our approach to calculate Raman scattering intensities. In graphene-based materials in equilibrium geometry, the off-diagonal components of the dielectric tensor are zero. Since only the in-plane component contributes to Raman scattering due to the symmetry of the phonons, the out-of plane component is not discussed here.

For graphene, the dielectric function is calculated from TDDFT within RPA, as well as by diagonalizing the full BSE Hamiltonian. The results are shown in Fig. 5.2. In the low energy region ($E < 5$ eV), where contributions mainly come from transitions between the π and π^* bands, the most important spectral features are already captured within RPA. In the literature, there are contradictory opinions about the role of excitonic effects in this energy region. While in Ref. [49], the peak in the imaginary part of the dielectric function at ≈ 4 eV is vanishing when including excitonic effects, in Refs. [54] and [25], it is argued, that only the shape and position of the peak change. In our calculation, only slight differences are found between the BSE and RPA results. We expect only a minor influence on the Raman spectra. In the high energy region excitonic effects play a more significant role. Especially the peak in the imaginary part at ≈ 12 eV is shifted to higher energies and has a different shape within TDDFT. As in Raman experiments usually laser energies in the visible or near UV region are used, the description within RPA is sufficient for our purpose.

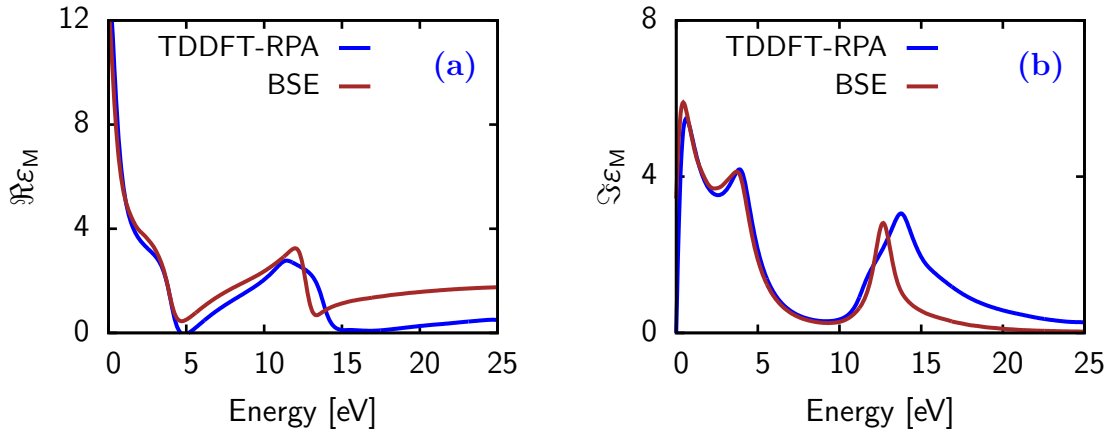


Figure 5.2: (a) Real and (b) imaginary part of the in-plane component of the dielectric function of graphene calculated with TDDFT within RPA and by diagonalizing the full BSE Hamiltonian.

The dielectric function of AB bilayer graphene and AB graphite (Figs. 5.3b and 5.3c) are very similar to the dielectric function of monolayer graphene. In AA graphite (Fig. 5.3a), the relative intensities of the two low-energy peaks of the imaginary part of the dielectric function are interchanged compared to the others. More information about the dielectric function of graphene-based materials can be found in Refs. [53] [38] and [26].

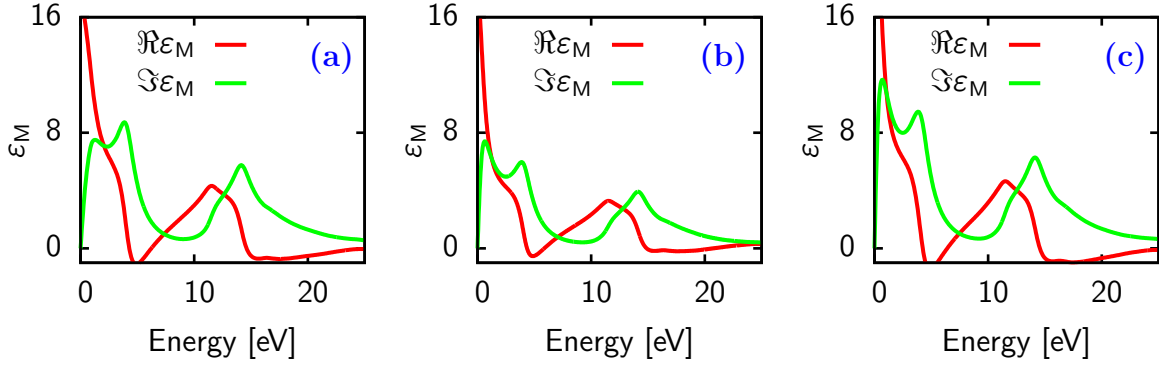


Figure 5.3: In-plane component of the dielectric function of (a) AA graphite, (b) AB bilayer graphene and (c) AB graphite from TDDFT within RPA.

5.4 Phonons

The phonon dispersions of graphene and AA graphite are characterized by in-plane and out-of-plane modes. The phonon-dispersion curve of graphene obtained with PBE is presented in Fig. 5.4. Figs. 5.5a and 5.5b show the LDA dispersion curves of graphene and AA graphite. Because of the two atoms in the unit cell, there are six phonon bands belonging to longitudinal optical (LO), in-plane transversal optical (iTO), out-of-plane transversal optical (oTO), longitudinal acoustical (LA), in-plane transversal acoustical (iTA), and out-of-plane transversal acoustical (oTA) vibrations. For both optical and acoustical phonons within the whole BZ, frequencies of the in-plane modes are higher than for the corresponding out-of-plane ones.

Kohn anomalies appear in the dispersion of the highest phonon mode at both the Γ point (LO mode) and at the K point (iTO mode), due to strong electron-phonon coupling. At Γ point, the behavior is well-described within DFT, while, using local XC potentials, at the K point, the slope is underestimated. It was shown, that the slope in the dispersion is proportional to the square of the electron-phonon coupling constant [34]. In DFT, the electron-phonon coupling for iTO phonons at K is underestimated [20]. Using the electron-phonon coupling constant calculated within GW, the slope is renormalized by almost 80 % and phonon-dispersion curves in good agreement with experimental inelastic x-ray scattering data are obtained [20]. Apart from the iTO phonons near the K-point, the overall agreement between DFT, and experimental phonons frequencies is very good. While within LDA the frequencies are typically overestimated by $\approx 1\%$, within PBE they are underestimated by $\approx 1\%$.

Phonon-dispersion curves of bilayer graphene and AB graphite are presented in Figs. 5.5c and 5.5d. As both materials have four atom in the unit cell, there are 12 phonon bands. Due to the weak interlayer interaction, every phonon mode of graphene is split up into two phonon modes belonging to in-phase and out-of-phase vibrations of the sub-lattices. The frequencies of these modes are nearly degenerate, except for the oTA modes near the Γ point, where the splitting is much larger.

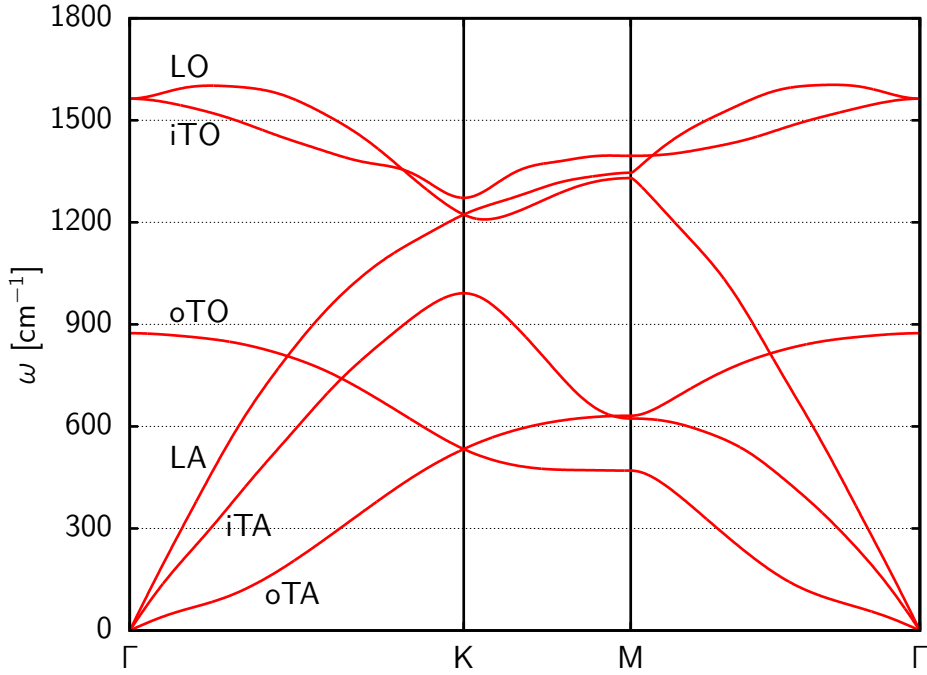


Figure 5.4: Phonon-dispersion curves of graphene, obtained with the XC-functional PBE. Labels stand for longitudinal optical (LO), in-plane transversal optical (iTO), out-of-plane transversal optical (oTO), longitudinal acoustical (LA), in-plane transversal acoustical (iTA), and out-of-plane transversal acoustical (oTA).

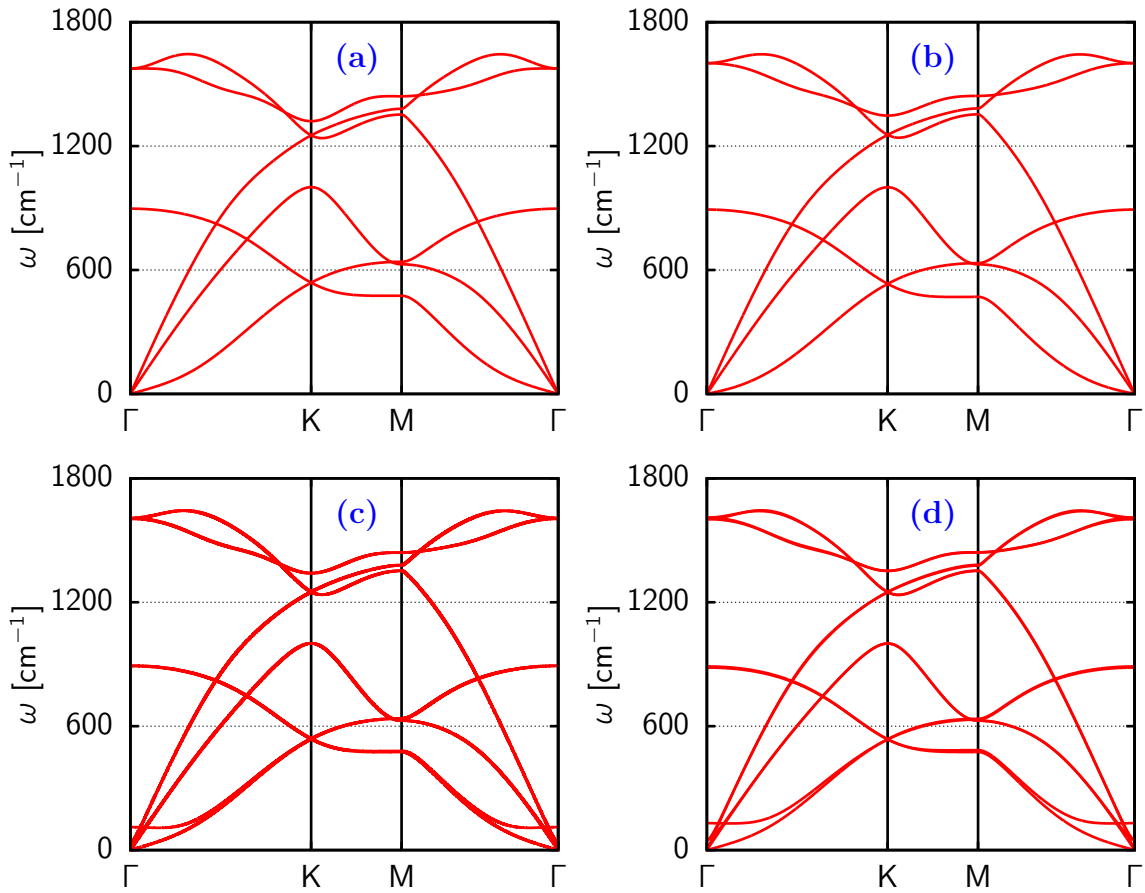


Figure 5.5: Phonon-dispersion curves of (a) graphene, (b) AA graphite, (c) AB bilayer graphene, and (d) AB graphite, using LDA.

Chapter 6

First-order Raman spectra: The G-band

In this chapter, the calculated first-order Raman spectra are presented. In Section 6.1, we show how the spectrum of graphene is obtained. In Section 6.2, the results for the graphene-based materials with different stacking arrangement are presented.

The number of peaks in a first-order Raman spectrum is limited by the number of phonon modes, which are Raman active by symmetry. In graphene and AA graphite, the degenerate in-plane optical Γ -point phonons have E_{2g} symmetry and are thus first-order Raman active. This leads to a single first-order peak in the Raman spectrum, which is usually called G-band. In AB bilayer graphene and AB graphite, phonon modes split up into in-phase and out-of-phase vibrations of the layers. This leads to four Raman-active phonon modes: The high-energy in-phase and the low-energy out-of-phase modes. In this thesis, the low-energy modes are not considered.

While the position of the peaks in the first-order Raman spectra are determined by the phonon frequencies, the intensity is proportional to the absolute square of the first derivative of the dielectric function with respect to the phonon normal coordinates.

6.1 Graphene

In the following we present and discuss all the ingredients needed to compute first-order Raman spectra in graphene. Because of the degeneracy of the in-plane phonons at the Γ point, there is a degree of freedom for choosing the frozen-phonon displacements. Any vector consisting of in-plane displacements, where the two atoms in the unit cell are displaced in opposite direction, is an eigenvector of the dynamical matrix. In this thesis, two linearly independent displacements along the Cartesian x and y directions are used.

6.1.1 Dielectric function of displaced structures

For calculating the first derivative of the dielectric function, atomic configurations are generated, in which the atoms are displaced along the phonon eigendisplacements. The absolute amount of displacement is given by the sum of the amplitudes

of the displacements of all atoms in one unit cell:

$$d = \sum_{\alpha} |\mathbf{u}_0^{\alpha}|. \quad (6.1)$$

With a step size of 0.01 Bohr in both positive and negative direction nine configurations are generated, leading to a maximum displacement $d = 0.04$ Bohr. The equilibrium structure and the displaced structures have different symmetry. For a good polynomial fit, only structures with the same symmetry should be used. Instead of the equilibrium geometry, a structure slightly displaced by 2×10^{-4} Bohr is used.

The out-of-plane component of the dielectric function is not affected by the in-plane displacement of the atoms. While for a displacement along the x direction the off-diagonal in-plane components change, the diagonal components of ϵ_M are affected by a displacement along y . For both types of displacements, changes appear in the whole optical region. The dielectric function of the equilibrium geometry and a displaced structure is shown in Fig. 6.1a (real part) and Fig. 6.1b (imaginary part). As can be seen in Figs. 6.1c and 6.1d, the imaginary part of the dielectric function is shifted by a constant over a wide range, while in the real part there is a crossing between 2 and 3 eV.

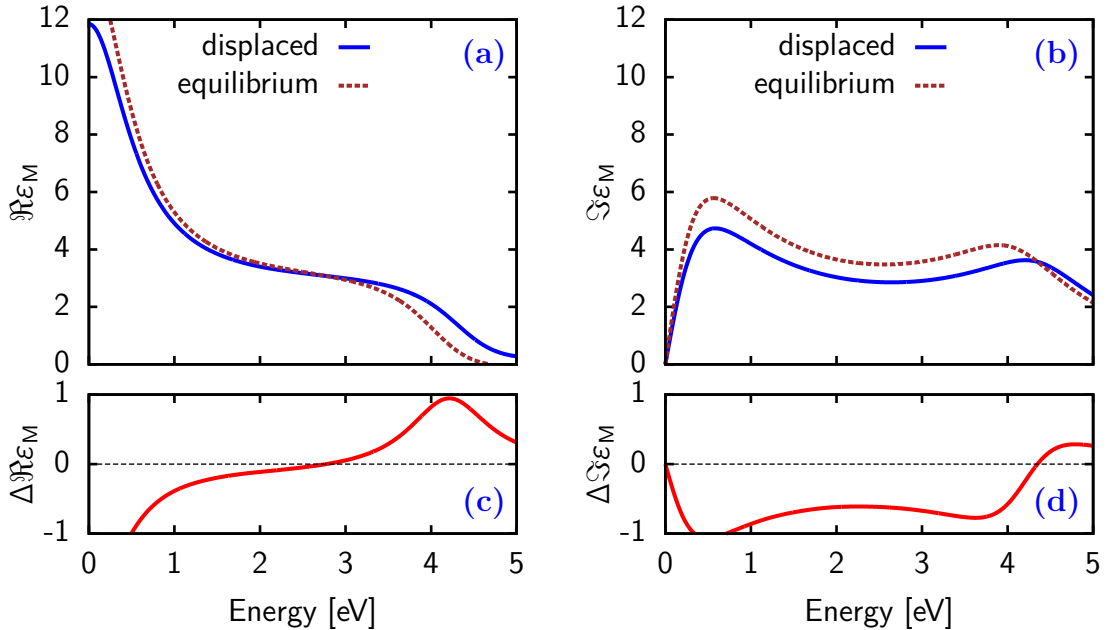


Figure 6.1: Diagonal in-plane component of the dielectric function. Real (a) and imaginary (b) part for equilibrium structure and a structure with atoms displaced along the y direction. Difference between displaced and equilibrium structure for real (c) and imaginary (d) part of the dielectric function. The dashed lines at zero difference are guides to the eye.

The first derivative of the dielectric function is obtained at each excitation energy from a quadratic fit of the dielectric function over the displacement, which is visualized for the energy of 1.2 eV in Fig. 6.2.

The choice of the XC potential has only little effect on the dielectric function and its derivative. As a consequence, also the Raman scattering intensity is unaffected by the choice of the XC potential. The optical phonon frequencies at the Γ point, on the other hand, differ by $\approx 2.5\%$. This leads to a shift of the G-band from

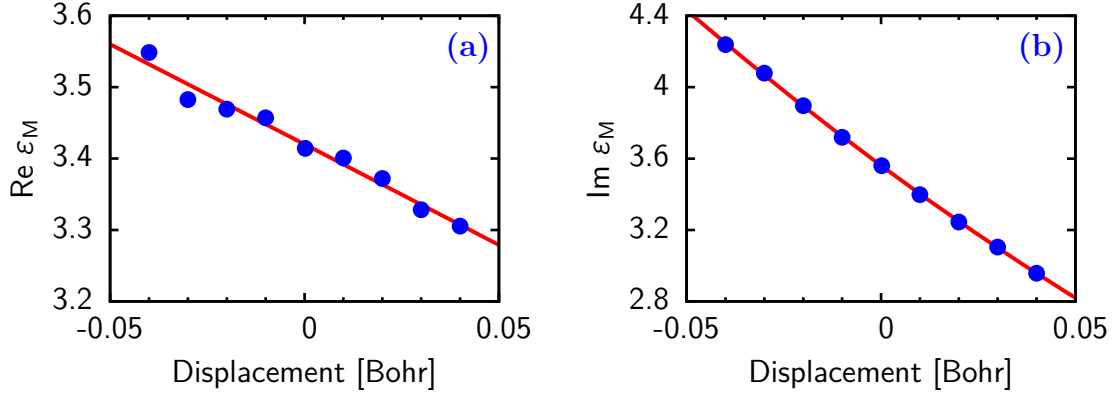


Figure 6.2: Real (a) and imaginary (b) part of the dielectric function at 1.2 eV of graphene for displaced structures. The red line is a quadratic fit for calculating the first derivative.

$\approx 1560 \text{ cm}^{-1}$ in PBE to $\approx 1600 \text{ cm}^{-1}$ in LDA. As we will see in the following, this affects the details of the results, but not its essence.

6.1.2 Raman spectra

The Raman-scattering efficiency is calculated from the first derivatives of the dielectric function and the phonon frequencies using Eq. (4.26). To obtain the Raman spectrum (Fig. 6.3), a Lorentzian broadening of 3 cm^{-1} is applied to the absolute Raman-scattering efficiency. As a direct result of the different LDA and PBE phonon frequencies, the peak is at different positions.

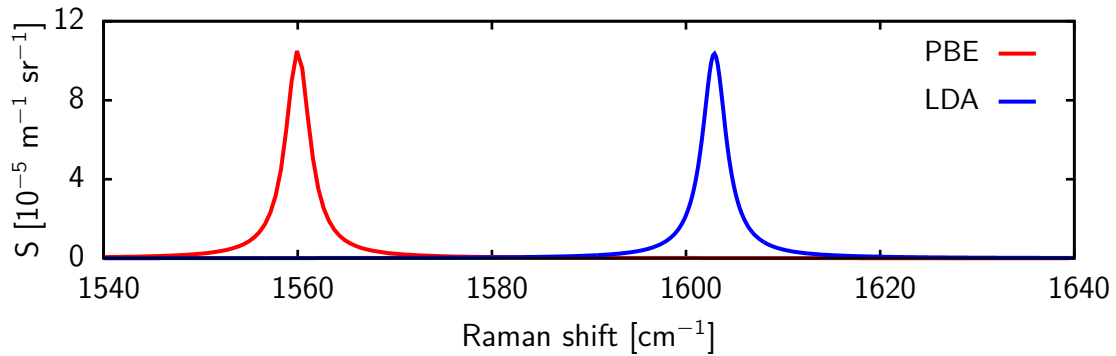


Figure 6.3: First-order Raman G-band of graphene obtained with PBE and LDA XC functionals.

6.1.3 Resonance behavior

In the absence of resonances, the energy dependence of Raman spectra is typically given by the energy prefactor $\omega_L \omega_s^3$. For investigating the resonance behavior, we look at the absolute square of the derivative of the dielectric function (Fig. 6.4) leaving aside the prefactor for a moment. In the G-band, no resonance appears in the optical region. The Raman scattering intensity is dominated by the energy

prefactor in Eq. (4.26), in agreement with experiment [3]. There is a resonance in the Raman spectrum in the UV region at ≈ 3.8 eV enhancing the intensity by a factor 2.5 compared to the non-resonant level at ≈ 2 eV. In the IR region the intensity is strongly enhanced.

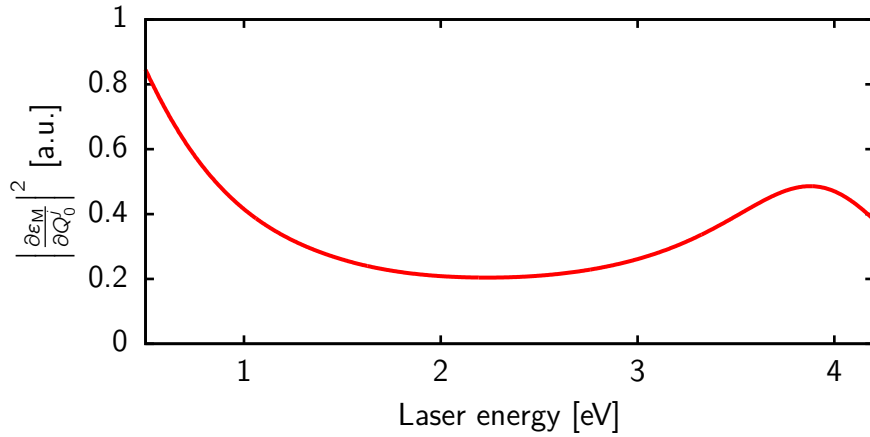


Figure 6.4: Absolute square of the derivative of the dielectric function of graphene. In the optical region, no resonance appears.

6.2 Other graphene-based materials

The procedure described in Section 6.1 is also applied to AB bilayer graphene and AA and AB graphite using the LDA XC functional. As the results are not essentially different, only the Raman spectrum is shown here. The G-band of all materials is shown in Fig. 6.5.

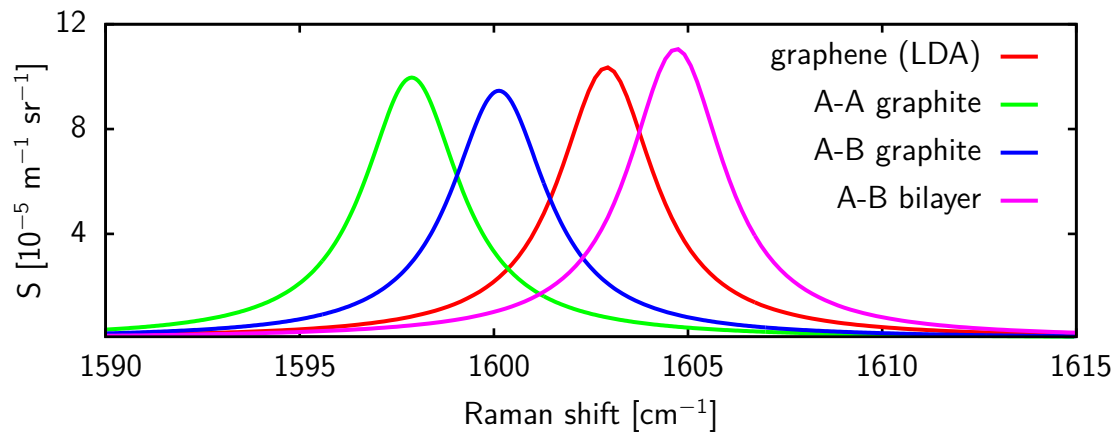


Figure 6.5: First-order Raman G-band of graphene-based materials using only LDA.

The stacking of graphene-layers has an effect on the Γ -point phonon frequencies and thus the position of the G-band in the Raman spectrum.

Chapter 7

Second-order Raman spectra: The 2D-band

In this chapter, second-order Raman spectra for graphene-based materials are presented. Calculations for graphene (Section 7.1) are done using the PBE and LDA XC functionals, while for calculations on AA graphite (Section 7.2), AB bilayer graphene (Section 7.3), and AB graphite (Section 7.4) only LDA is used.

Unlike first-order Raman spectra, many phonons contribute to second-order Raman spectra. In many materials, this leads to a broad spectrum. In graphene-based materials, the situation is different. For a given excitation energy, there are resonant contributions from a few phonon modes, which dominate the spectrum, leading to sharp peaks in the spectrum.

Second-order Raman calculations can become computationally very demanding mainly because of three reasons: i) Many individual calculations of the dielectric function are required; ii) Large supercells with many atoms are necessary, depending on the phonon \mathbf{q} -point; iii) A very smooth dielectric function is necessary for a good polynomial fit for calculating the derivatives. To keep the numerical effort feasible, we concentrate on the most relevant contributions to the second-order 2D-band, which come from overtones of the iTO phonons along the Γ -K path through the BZ (see Fig. 7.1), as was shown in Ref. [51]. For \mathbf{q} -points on this path, we introduce a short notation

$$\mathbf{q} = \lambda \mathbf{K} = \lambda \left(\frac{1}{3}, \frac{2}{3} \right), \quad (7.1)$$

where λ is the fraction of the distance between Γ and K. Here the coordinates of the K-point in reciprocal lattice vectors from Fig. 1.1b are used.

For all systems, calculations at \mathbf{q} -points between $\frac{3}{5}\mathbf{K}$ and $\frac{6}{7}\mathbf{K}$ have been performed. Instead of taking equidistant \mathbf{q} -points, the \mathbf{q} -points with the smallest commensurate supercells are chosen (see Tab. 7.1). For calculations on monolayer graphene with PBE XC-functional, four points in between are used. For AB graphite only one point in between is used, while for all other calculations two points in between are used.

7.1 Graphene

In this section, the second-order Raman spectrum of graphene is presented. The dielectric function of structures with atoms displaced along the phonon normal coordinates is analyzed, and the spectrum is calculated by using Gaussians for the

\mathbf{q} [K]	\mathbf{q} [rec. lattice vectors]	N_{SC}	systems
$\frac{3}{5}$	$(\frac{1}{5}, \frac{2}{5})$	5	all
$\frac{2}{3}$	$(\frac{2}{9}, \frac{4}{9})$	9	all except AB graphite
$\frac{9}{13}$	$(\frac{3}{13}, \frac{6}{13})$	13	graphene PBE
$\frac{3}{4}$	$(\frac{1}{4}, \frac{1}{2})$	4	all
$\frac{9}{11}$	$(\frac{3}{11}, \frac{6}{11})$	11	graphene PBE
$\frac{6}{7}$	$(\frac{2}{7}, \frac{4}{7})$	7	all

Table 7.1: \mathbf{q} -points for second-order Raman calculations. In the first two columns, the \mathbf{q} -point is given as a fraction of the distance between the Γ and K point, and in reciprocal lattice vectors. N_{SC} is the number of unit cells in the supercell commensurate with \mathbf{q} . The last column gives the systems for which calculations at this \mathbf{q} -point have been done.

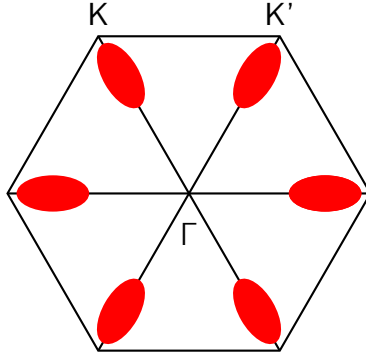


Figure 7.1: First BZ of graphene. The \mathbf{q} -points, for which calculations are done are in the regions marked in red.

interpolation along the Γ -K path.

7.1.1 Dielectric function of displaced structures

For second-order Raman spectra, we need to calculate the second derivative of the dielectric function with respect to the phonon normal coordinates. For this purpose nine structures with displaced atoms are constructed. The absolute amount of displacement is given by the sum of the amplitudes of the displacements of all atoms per unit cell:

$$d = \frac{1}{N_{SC}} \sum_{\alpha} \sum_{l \in SC} |\mathbf{u}_l^{\alpha}|. \quad (7.2)$$

Displacements in both positive and negative direction are used with a step size of 0.01 Bohr. Like for the first-order calculation, the equilibrium geometry is replaced by a structure with a small displacement of 2×10^{-4} Bohr.

Unlike in the last chapter, the dielectric function is only minimally affected by the displacements in most of the considered energy range. In small regions, dependent on the \mathbf{q} -point, the shift is larger (see Fig. 7.2).

For the evaluation of the second derivative, at each excitation energy a fourth-order polynomial fit is used. As shown in Fig. 7.3, the equilibrium structure is at an extremity of both the imaginary and real part of the dielectric function. As a result,

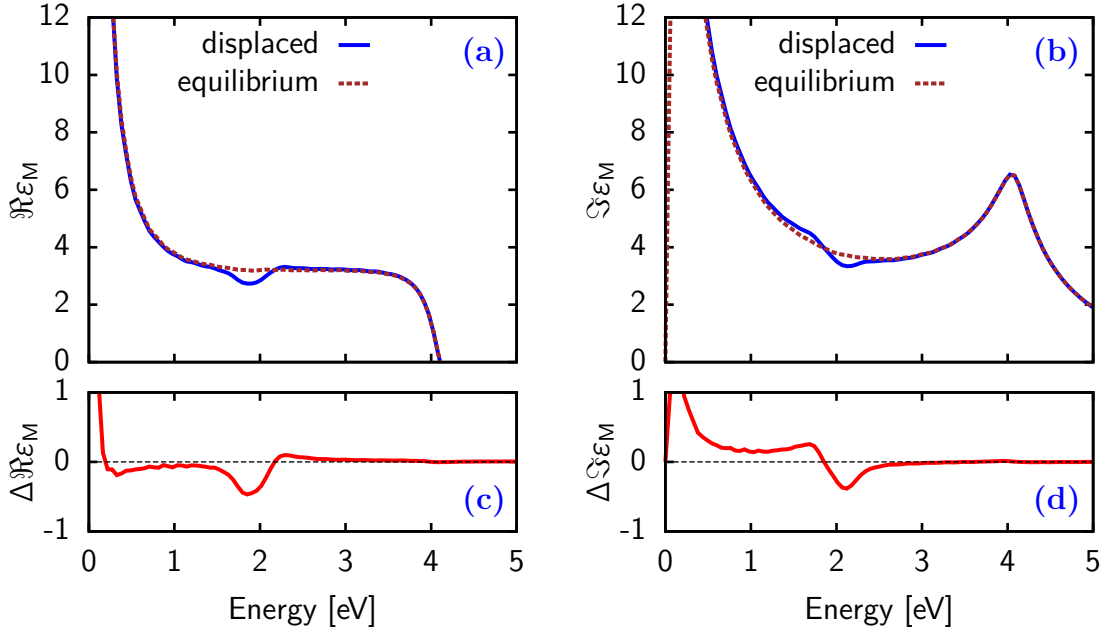


Figure 7.2: Real (a) and imaginary (b) part of the dielectric function of graphene in equilibrium structure and a structure with atoms displaced along the iTO phonon normal coordinates at $\mathbf{q} = \frac{3}{4}K$. Difference between displaced and equilibrium structure for real (c) and imaginary (d) part of the dielectric function. The dashed lines at zero difference are guides to the eye.

the linear fitting coefficient is zero. This is expected, as the linear term belongs to first-order processes, which are forbidden due to momentum conservation laws.

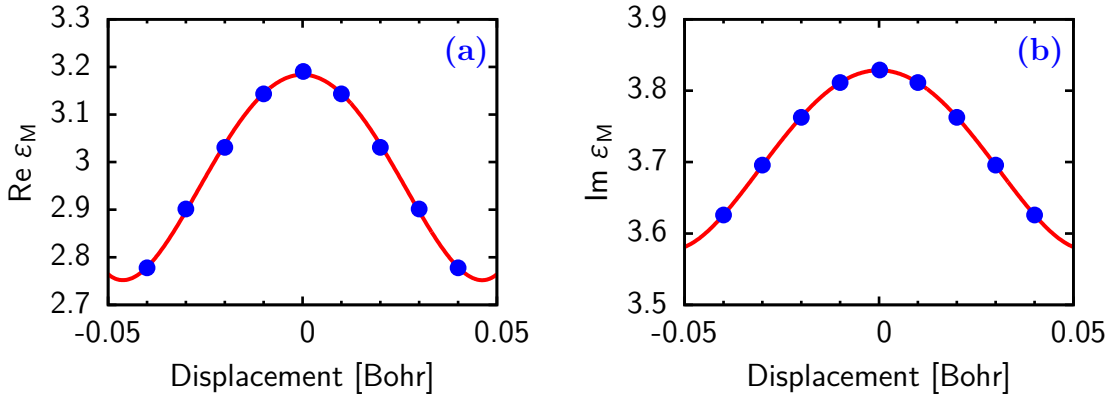


Figure 7.3: Real (a) and imaginary (b) part of the dielectric function as a function of the displacement. The red line is a fourth-order polynomial fit. The excitation energy is at resonance.

The second derivatives of the dielectric function with respect to the iTO phonon normal coordinates show resonances in the energy ranges where the dielectric function exhibits a dependence on the displacements as described above. The positions of these resonances change with the phonon momentum (see Fig. 7.4). A trivial interpolation of the second derivatives over the BZ for each excitation energy will thus not reproduce the correct energy dependence of the second derivatives. The

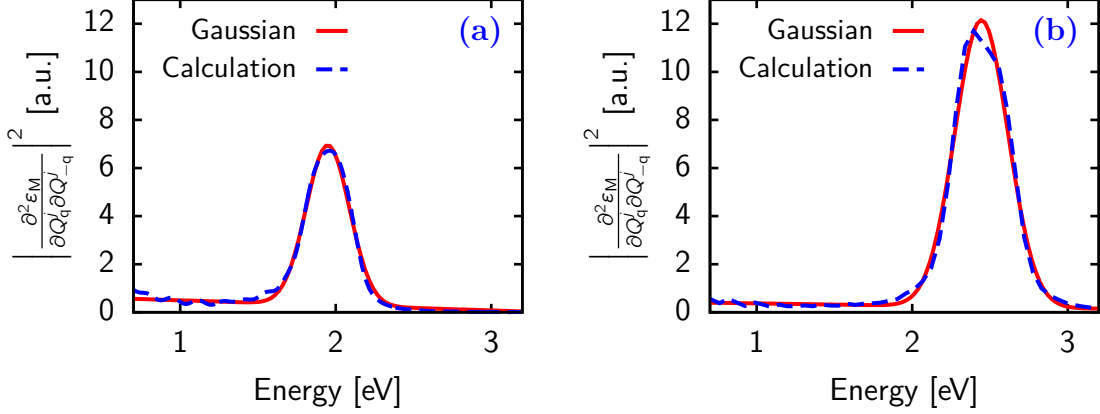


Figure 7.4: Absolute square of the second derivatives of the dielectric function with respect to the iTO phonon normal coordinates at $\mathbf{q} = \frac{3}{4}\text{K}$ (a) and $\mathbf{q} = \frac{2}{3}\text{K}$ (b). The dashed blue curves correspond to values calculated within the frozen-phonon approximation, while the red line is a Gaussian plus a linear background fit.

overall shape of the resonances can be reproduced, however, by a Gaussian of the type

$$G(x) = \frac{A}{\sigma\sqrt{2\pi}} e^{-\frac{(x-x_0)^2}{2\sigma^2}}. \quad (7.3)$$

For this reason, the absolute square of the dielectric function derivatives as a function of excitation energy is fitted using a Gaussian function as in Eq. (7.3). For a better simulation of the non-resonant part of the second derivatives of the dielectric function, a linear background is added. Instead of interpolating the derivatives of the dielectric function directly, the position x_0 , width σ , and intensity A obtained from the Gaussian fit are used. As we are only interested in the resonant part of the Raman spectrum, the linear background is left out of the interpolation.

Figure 7.5 shows the parameters of the Gaussians along the Γ -K path for LDA and PBE calculations. The position, as well as the width and intensity of the Gaussians decreases monotonously with the phonon momentum. Overall, the LDA and PBE calculations lead to very similar results. The positions of the peaks are in good agreement, while the widths and intensities are only slightly different.

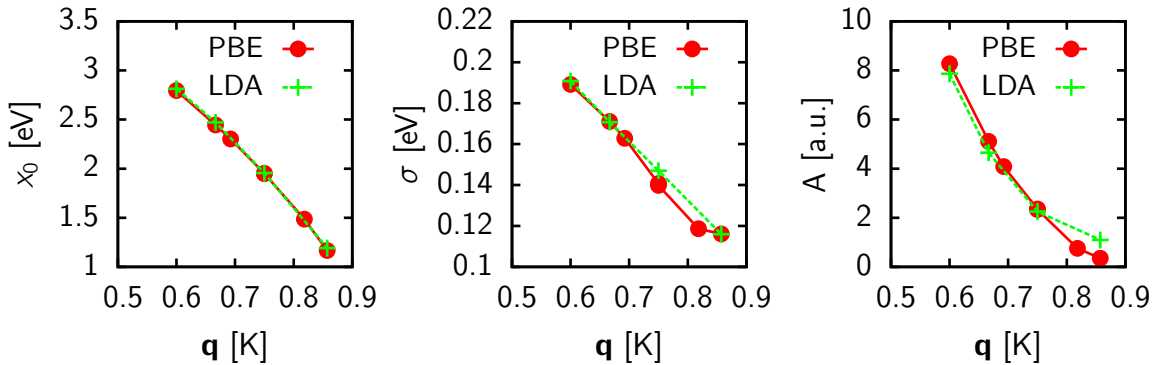


Figure 7.5: Position x_0 , width σ , and intensity A of resonances of the iTO phonon modes along Γ -K, calculated with PBE (red) and LDA (green).

7.1.2 Raman spectrum

The contributions to the second-order Raman spectrum from overtones of the iTO phonons along Γ -K are calculated from the interpolated values of the second derivative of the dielectric function using Eq. (4.27). The spectra obtained for the excitation energies 1.6 eV, 2.0 eV, and 2.4 eV are shown in Fig. 7.6a.

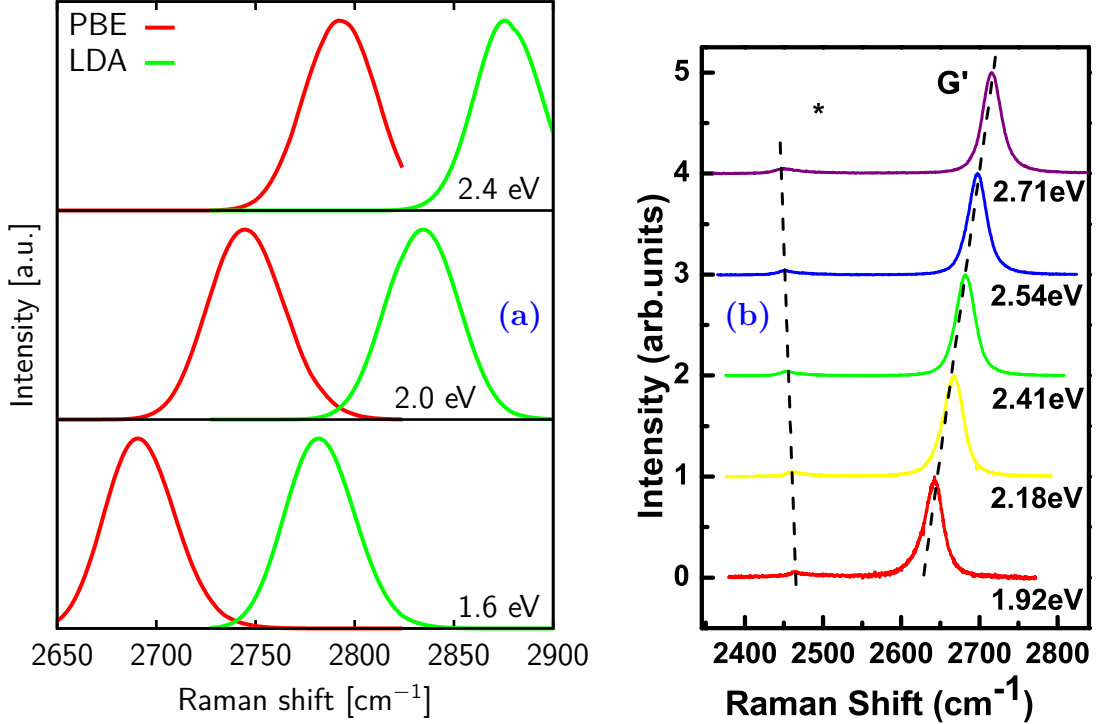


Figure 7.6: (a) Second-order 2D-band of monolayer graphene for excitation energies of 1.6, 2.0, and 2.4 eV. The XC functionals used are PBE (red lines) and LDA (green lines). (b) Experimental second-order spectrum of graphene for different laser energies from Ref. [24].

The 2D-band is dispersive. The frequency of the band maximum increases with the laser energy by $120 \text{ cm}^{-1}\text{eV}^{-1}$. Compared to the experimental value from Ref. [24] ($88 \text{ cm}^{-1}\text{eV}^{-1}$), the dispersion is somewhat overestimated.

7.2 AA graphite

Like monolayer graphene, AA graphite has 2 atoms in the unit cell. Both materials have similar electronic and vibrational properties. This leads to very similar second-order Raman spectra. For comparison, we plot both spectra in Fig. 7.7. The resonances in the second derivatives of the dielectric function of AA graphite show almost exactly the same behavior as the ones of graphene. In the DFT phonon dispersion of AA graphite (Fig. 5.5b), the Kohn anomaly at K is reduced compared to graphene. This leads to a larger Raman shift at the 2D maximum for small excitation energies. For higher energy (2.4 eV), the spectra are almost identical.

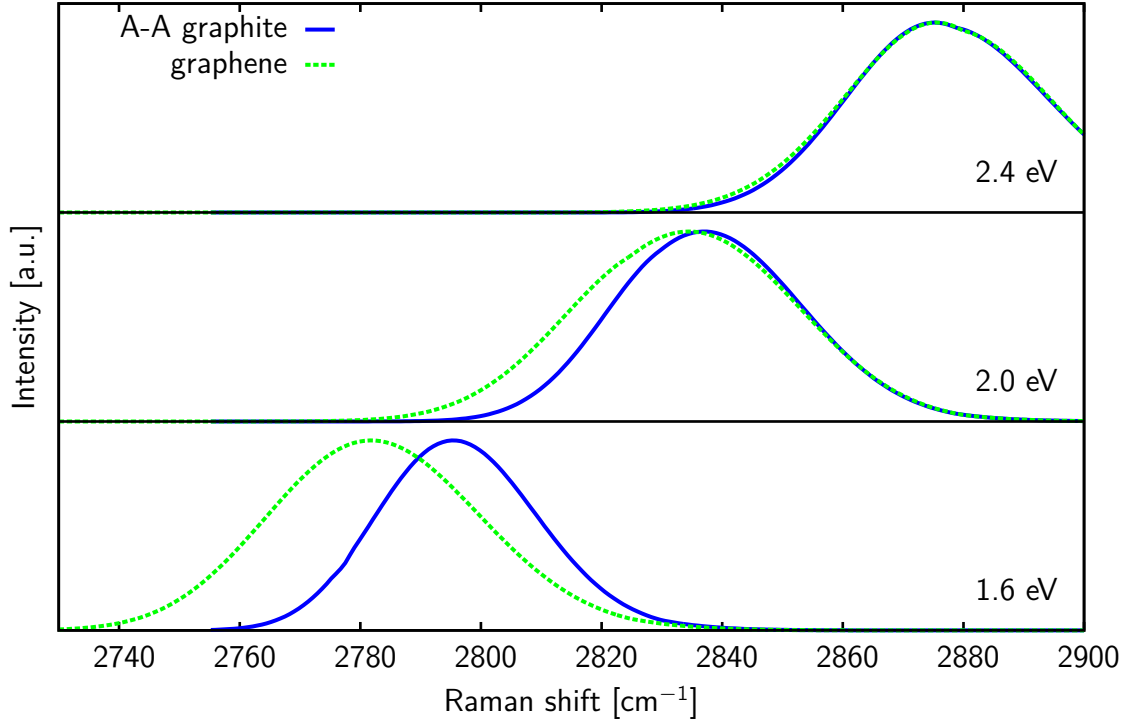


Figure 7.7: Second-order 2D-band of AA graphite and graphene for excitation energies of 1.6, 2.0, and 2.4 eV.

7.3 AB bilayer graphene

In AB bilayer graphene, the situation is more complex. Because of the doubled number of atoms in the unit cell, there are two almost degenerate iTO phonon bands. There are resonant contributions from both bands to the second-order Raman spectrum.

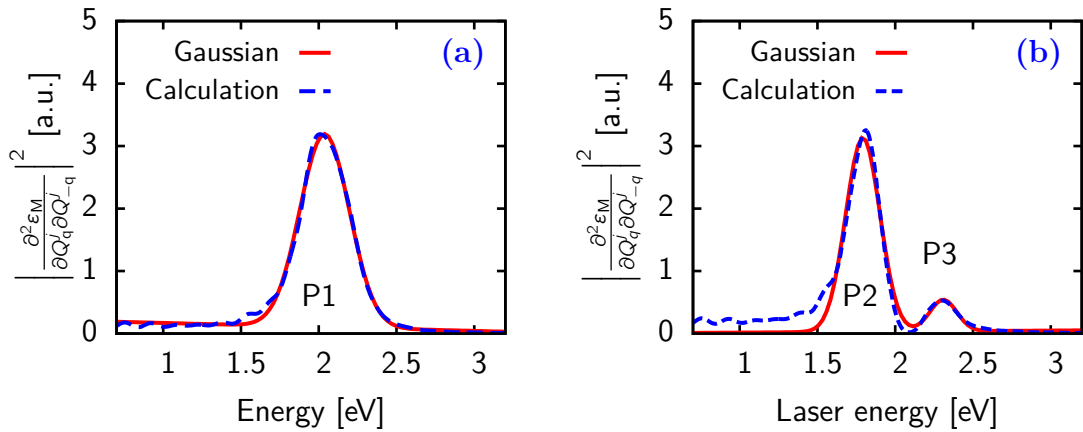


Figure 7.8: Absolute square of the second derivatives of the dielectric function with respect to the phonon normal coordinates of the higher (a) and lower (b) iTO phonons. The red lines correspond to fits using one (a) and two (b) Gaussians.

The second derivatives of the dielectric function with respect to the normal coordinates of the higher phonon band (Fig. 7.8a) show a behavior, similar to the

one in graphene and AA graphite. There is one resonance, labeled P1, which is slightly shifted up in energy compared to graphene. This allows us to apply the method of Gaussian fitting used so far also for this band. In the second derivatives with respect to the lower iTO phonon normal coordinates (Fig. 7.8b), there are two resonances. The one labeled P2 is lower, the other one (P3) is higher in energy than P1. For the corresponding second derivatives, a fit consisting of two Gaussians plus a linear background is used. The parameters of all three Gaussians along Γ -K are shown in Fig. 7.9.

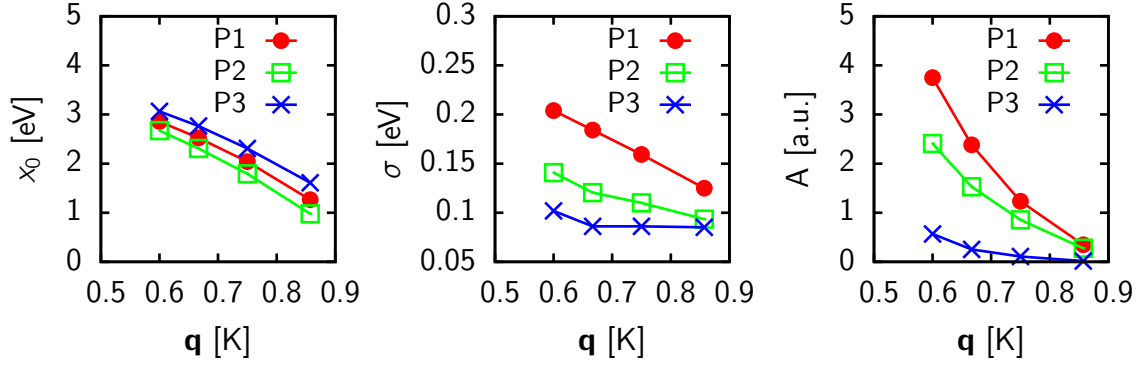


Figure 7.9: Position x_0 , width σ , and intensity A of resonances of the iTO phonon modes along Γ -K. The resonances are labeled as in Fig. 7.8.

For the second-order Raman spectrum of AB bilayer graphene (Fig. 7.10), the contributions of all three resonances are summed according to Eq. (4.27). As the splitting of the iTO phonon bands cannot be estimated with the available data, the averaged value of both phonon bands is used.

The 2D-band of bilayer graphene is dispersive like in monolayer graphene. Its shape is characterized by the weights and widths of the three peaks making up the full feature. For all excitation energies, the peak lowest in energy (P3) has the smallest contribution. When going from lower to higher laser energies, the relative weight of the peak at the highest frequency (P2) is increasing, in good agreement with experimental data [7][14] and calculations based on the DR approach [14].

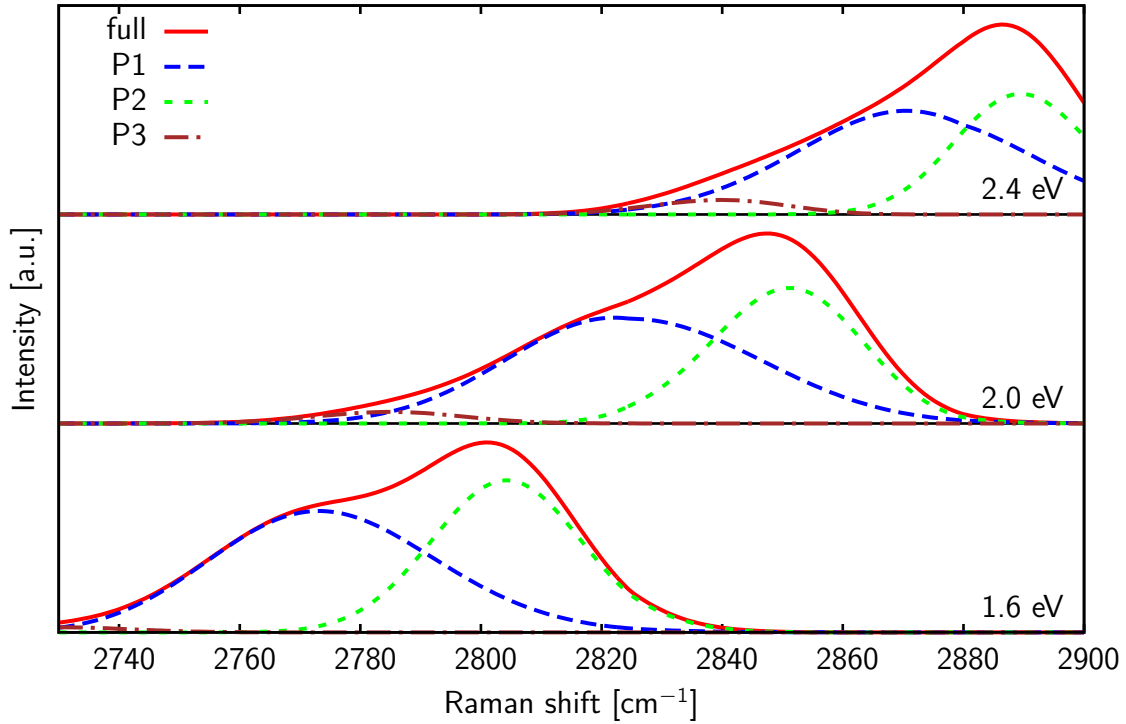


Figure 7.10: Second-order 2D-band of AB bilayer graphene for different excitation energies decomposed into its contributions.

7.4 AB graphite

The electron and phonon properties of AB graphite are similar to the ones of AB bilayer graphene. Like in bilayer graphene, there are two main contributions from the lower iTO phonon band (P2 and P3) and one contribution from the higher iTO band (P1). In AB graphite, however, there is a larger discrepancy between the shape of the resonances and the Gaussians. Compared to bilayer graphene, the resonance P3 is even lower in intensity. Still, around the maximum of the resonances, the description is good enough to capture the most important effects. The evolution of the Gaussians along Γ -K is shown in Fig. 7.11.

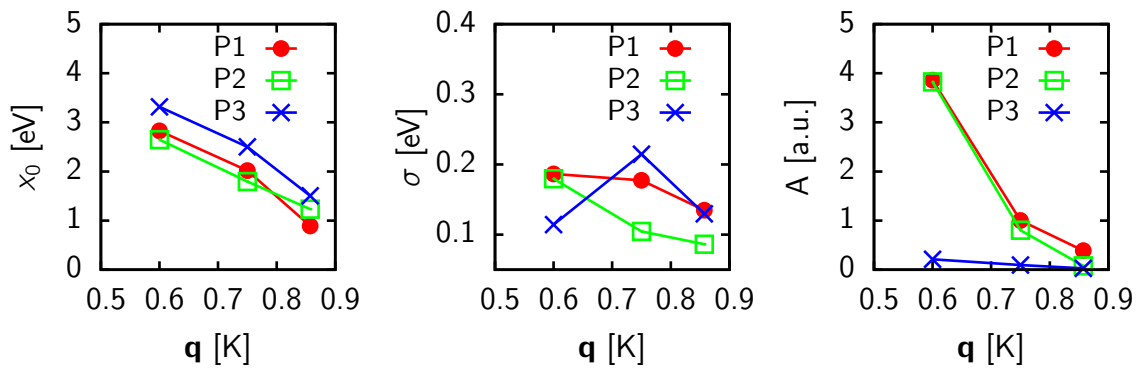


Figure 7.11: Position, width, and intensity of resonances of the iTO phonon modes along Γ -K for AB graphite.

In AB graphite, the Gaussians show an interesting behavior at \mathbf{q} -points near K. In bilayer graphene, and in AB graphite for the two \mathbf{q} -points away from K,

the position of resonance P1 is between P2 and P3. However at $\mathbf{q} = \frac{6}{7}\mathbf{K}$, P1 is the resonance at highest energy. This leads to a point in between, where both resonances contribute at the same frequency to the Raman spectrum. To further investigate this behavior, calculations for more \mathbf{q} -point in between would be necessary.

The second-order Raman spectrum with the individual contributions of the three resonances is shown in Fig. 7.12. Like for AB bilayer graphene, the splitting of the phonon bands is neglected. For an excitation energy of 1.6 eV, P1 and P2 are close together. For higher energies, the peaks shift away from each other. The contribution from P3, which is already small in bilayer graphene, is almost invisible in the Raman spectrum of AB graphite.

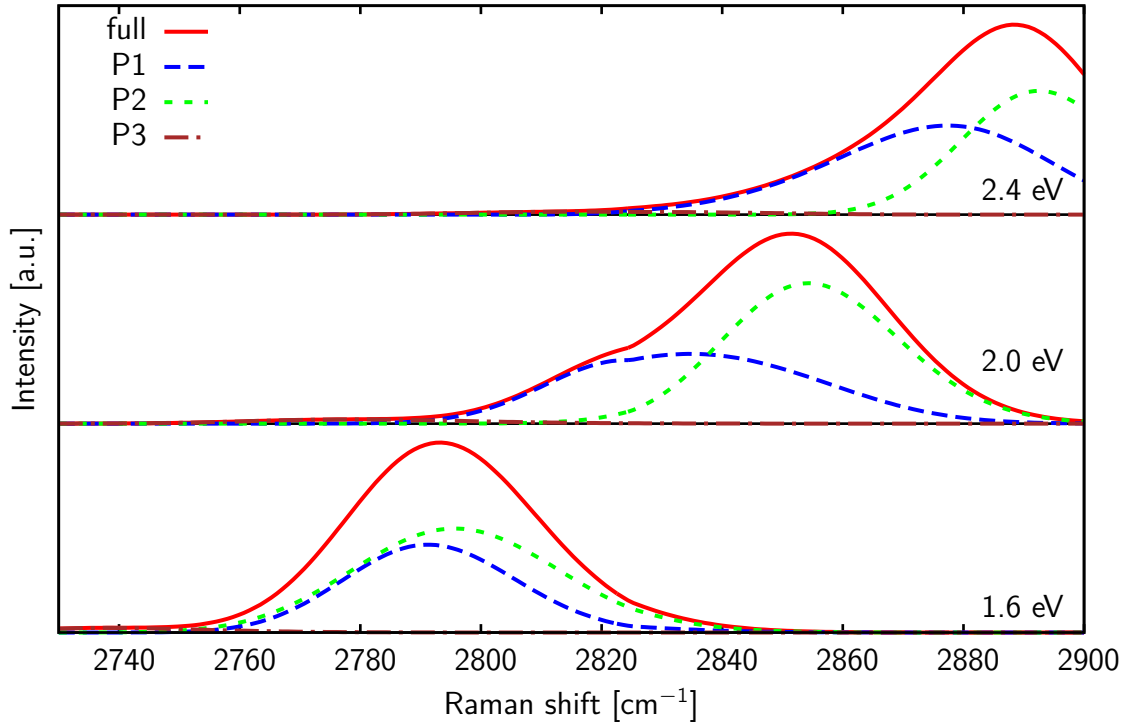


Figure 7.12: Second-order 2D-band of AB graphite for different excitation energies.

7.5 Effect of layer stacking

The second-order Raman spectra for all four materials are compared to each other in Fig. 7.13 for an excitation energy of 2.0 eV. The 2D band of monolayer graphene and AA graphite have a small width, as both spectra are made up by a single contribution. In AA graphite, the peak is at slightly higher Raman shift, due to higher iTO phonon frequencies around K. The 2D-bands of AB bilayer graphene and AB graphite are much broader. Both are built up from three individual contributions. Compared to experimental data [7], the intensity of the lowest peak is underestimated in both cases. The reason for this might be the restriction to contributions from phonons along Γ -K.

The weights and positions of the individual contributions to the spectra of the AB stacked materials are different. In AB graphite, the two main peaks are closer together, leading to a sharper main peak compared to AB bilayer graphene.

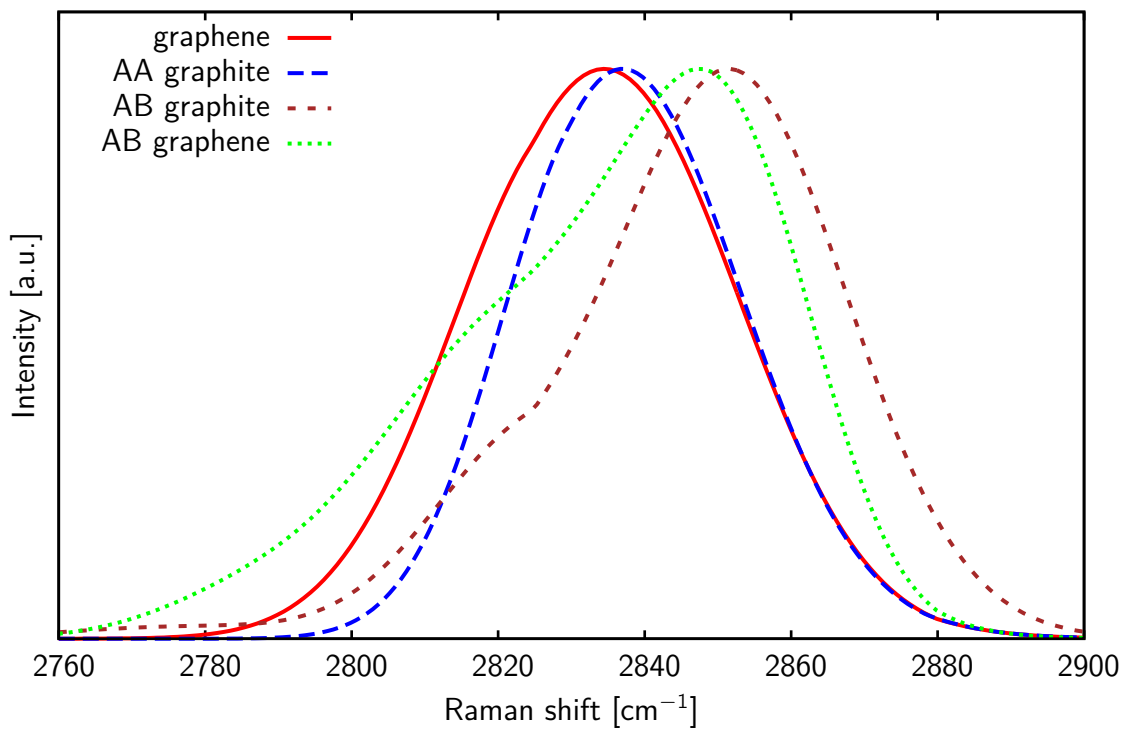


Figure 7.13: Second-order 2D-band of graphene-based materials at an excitation energy of 2.0 eV.

Chapter 8

Conclusions and outlook

In the present work, first- and second-order Raman spectra of graphene-based materials were calculated. A part of the work done for this thesis was the extension of an already existing implementation of first-order Raman scattering in the DFT package **exciting** to the second order. Calculations were performed for monolayer graphene, AA graphite, AB bilayer graphene, and AB graphite. Prior to the calculation of Raman scattering intensities, structural, electronic, optical and vibrational properties of the materials were obtained.

The prominent first-order Raman feature of graphene-based materials is the G-band. For monolayer graphene, it was shown, that the XC functional has only a small influence on the intensity of the Raman spectrum, while the position of the G-band changes, due to a dependence of the phonon frequencies on the XC potential. While the G-band is at $\approx 1600 \text{ cm}^{-1}$ for LDA calculations, it is at $\approx 1560 \text{ cm}^{-1}$ when using PBE. The experimental value is in between, *i.e.* at $\approx 1580 \text{ cm}^{-1}$. The G-band position is shifted with the amount depending on the stacking sequence. In the optical region, the G-band is off-resonant, while the intensity is enhanced in the UV and IR region.

The second-order 2D-band at $\approx 2700 \text{ cm}^{-1}$ is often used to determine the number of layers in a sample of multilayer graphene. In this thesis, the effect of both the stacking sequence and excitation energy on the 2D-band was investigated. The 2D-band is dispersive. For higher excitation energies, it is shifted to higher frequencies. In monolayer graphene and AA graphite, the 2D-band consists of a single peak. The spectra of these two materials differ only because of small differences in the phonon dispersions they are based on. In the AB stacked materials, the broader 2D-band is made up by three peaks, which result from resonant contributions in both iTO phonon modes. The relative weights of the peaks of bilayer graphene and AB graphite are different and change with the excitation energy.

Based on the results shown in this thesis, there are many directions for further research. This includes the investigation of Raman spectra, which were not considered here: the first-order C-band from the degenerate low-energy optical in-plane phonons in bilayer graphene and AB graphite, as well as the low-intensity second-order lines. An improvement of the line-shape of the 2D-band can be achieved by extending the calculations to the full Brillouin zone. This will also allow for the calculation of absolute intensities of the 2D-band hence comparison to the G-band intensity.

The methodology developed and implemented in this thesis can be applied to a broader variety of materials. The family of graphene-based materials offers many

additional candidates. Other stacking possibilities include AA bilayer graphene, trilayer graphene, or ABC graphite. Furthermore, with carbon nanotubes and fullerenes, there are carbon allotropes with further reduced dimensionality, which would be exciting to explore. Other promising candidates are layered materials containing other elements, like silicene, germanene. An interesting question to be answered is, if the structural similarities of these materials to graphene lead to similar Raman spectra.

Bibliography

- [1] AMBROSCH-DRAXL, C. ; AUER, H. ; KOUBA, R. ; SHERMAN, E. Y. ; KNOLL, P. ; MAYER, M. : Raman scattering in $\text{YBa}_2\text{Cu}_3\text{O}_7$: A comprehensive theoretical study in comparison with experiments. In: *Phys. Rev. B* 65 (2002), Jan, 064501. <http://dx.doi.org/10.1103/PhysRevB.65.064501>. – DOI 10.1103/PhysRevB.65.064501
- [2] ANEES, P. ; VALSAKUMAR, M. C. ; CHANDRA, S. ; PANIGRAHI, B. K.: Ab initio study on stacking sequences, free energy, dynamical stability and potential energy surfaces of graphite structures. In: *Modelling and Simulation in Materials Science and Engineering* 22 (2014), Nr. 3, 035016. <http://stacks.iop.org/0965-0393/22/i=3/a=035016>
- [3] CANÇADO, L. G. ; JORIO, A. ; PIMENTA, M. A.: Measuring the absolute Raman cross section of nanographites as a function of laser energy and crystallite size. In: *Phys. Rev. B* 76 (2007), Aug, 064304. <http://dx.doi.org/10.1103/PhysRevB.76.064304>. – DOI 10.1103/PhysRevB.76.064304
- [4] CARDONA, M. : *Light Scattering in Solids I*. Springer-Verlag Berlin Heidelberg, 1983. <http://dx.doi.org/10.1007/3-540-11913-2>. <http://dx.doi.org/10.1007/3-540-11913-2>. – ISBN 978-3-540-70755-4
- [5] CASTRO NETO, A. H. ; GUINEA, F. ; PERES, N. M. R. ; NOVOSELOV, K. S. ; GEIM, A. K.: The electronic properties of graphene. In: *Rev. Mod. Phys.* 81 (2009), Jan, 109–162. <http://dx.doi.org/10.1103/RevModPhys.81.109>. – DOI 10.1103/RevModPhys.81.109
- [6] FERMI, E. ; RASETTI, F. : Über den Ramaneffekt des Steinsalzes. In: *Zeitschrift für Physik* 71 (1931), Sep, 689-695. <http://link.springer.com/article/10.1007/BF01339577>
- [7] FERRARI, A. C. ; MEYER, J. C. ; SCARDACI, V. ; CASIRAGHI, C. ; LAZZERI, M. ; MAURI, F. ; PISCANEC, S. ; JIANG, D. ; NOVOSELOV, K. S. ; ROTH, S. ; GEIM, A. K.: Raman Spectrum of Graphene and Graphene Layers. In: *Phys. Rev. Lett.* 97 (2006), Oct, 187401. <http://dx.doi.org/10.1103/PhysRevLett.97.187401>. – DOI 10.1103/PhysRevLett.97.187401
- [8] FERRARI ANDREA C. ; BASKO DENIS M.: Raman spectroscopy as a versatile tool for studying the properties of graphene. In: *Nat Nano* 8 (2013), apr, Nr. 4, 235-246. <http://dx.doi.org/http://dx.doi.org/10.1038/nnano.2013.46>. – DOI <http://dx.doi.org/10.1038/nnano.2013.46>. – ISSN 1748-3387. – 10.1038/nnano.2013.46

- [9] GILLET, Y. ; GIANTOMASSI, M. ; GONZE, X. : First-principles study of excitonic effects in Raman intensities. In: *Phys. Rev. B* 88 (2013), Sep, 094305. <http://dx.doi.org/10.1103/PhysRevB.88.094305>. – DOI 10.1103/PhysRevB.88.094305
- [10] GULANS, A. ; KONTUR, S. ; MEISENBICHLER, C. ; NABOK, D. ; PAVONE, P. ; RIGAMONTI, S. ; SAGMEISTER, S. ; WERNER, U. ; DRAXL, C. : exciting: a full-potential all-electron package implementing density-functional theory and many-body perturbation theory. In: *Journal of Physics: Condensed Matter* 26 (2014), Nr. 36, 363202. <http://stacks.iop.org/0953-8984/26/i=36/a=363202>
- [11] HANKE, W. ; SHAM, L. J.: Many-particle effects in the optical spectrum of a semiconductor. In: *Phys. Rev. B* 21 (1980), May, 4656–4673. <http://dx.doi.org/10.1103/PhysRevB.21.4656>. – DOI 10.1103/PhysRevB.21.4656
- [12] HAYES, W. ; LOUDON, R. : *Scattering of Light by Crystals*. Wiley, New York, 1978. – ISBN 0471031917
- [13] HELLER, E. J. ; YANG, Y. ; KOCIA, L. ; CHEN, W. ; FANG, S. ; BORUNDA, M. ; KAXIRAS, E. : Theory of Graphene Raman Scattering. In: *ACS Nano* 10 (2016), Nr. 2, 2803–2818. <http://dx.doi.org/10.1021/acsnano.5b07676>. – DOI 10.1021/acsnano.5b07676. – PMID: 26799915
- [14] HERZIGER, F. ; CALANDRA, M. ; GAVA, P. ; MAY, P. ; LAZZERI, M. ; MAURI, F. ; MAULTZSCH, J. : Two-Dimensional Analysis of the Double-Resonant 2D Raman Mode in Bilayer Graphene. In: *Phys. Rev. Lett.* 113 (2014), Oct, 187401. <http://dx.doi.org/10.1103/PhysRevLett.113.187401>. – DOI 10.1103/PhysRevLett.113.187401
- [15] HOHENBERG, P. ; KOHN, W. : Inhomogeneous Electron Gas. In: *Phys. Rev.* 136 (1964), Nov, B864–B871. <http://dx.doi.org/10.1103/PhysRev.136.B864>. – DOI 10.1103/PhysRev.136.B864
- [16] KNOLL, P. ; AMBROSCH-DRAXL, C. ; MIHAILOVIĆ, D. (Hrsg.): *Proceedings of the International Workshop on Anharmonic Properties of High- T_C Cuprates: Bled, Slovenia, September 1-6, 1994*. World Scientific <https://books.google.de/books?id=FRliQgAACAAJ>. – ISBN 9789810221805
- [17] KOHN, W. ; SHAM, L. J.: Self-Consistent Equations Including Exchange and Correlation Effects. In: *Phys. Rev.* 140 (1965), Nov, A1133–A1138. <http://dx.doi.org/10.1103/PhysRev.140.A1133>. – DOI 10.1103/PhysRev.140.A1133
- [18] LANDSBERG, G. S. ; MANDELSTAM, L. I.: Eine neue Erscheinung bei der Lichtzerstreuung in Krystallen. In: *Naturwissenschaften* 16 (1928), Nr. 28, 557–558. <http://dx.doi.org/10.1007/BF01506807>. – DOI 10.1007/BF01506807. – ISSN 1432–1904
- [19] LANGRETH, D. C. ; MEHL, M. J.: Beyond the local-density approximation in calculations of ground-state electronic properties. In: *Phys. Rev. B* 28 (1983), Aug, 1809–1834. <http://dx.doi.org/10.1103/PhysRevB.28.1809>. – DOI 10.1103/PhysRevB.28.1809

- [20] LAZZERI, M. ; ATTACCALITE, C. ; WIRTZ, L. ; MAURI, F. : Impact of the electron-electron correlation on phonon dispersion: Failure of LDA and GGA DFT functionals in graphene and graphite. In: *Phys. Rev. B* 78 (2008), Aug, 081406. <http://dx.doi.org/10.1103/PhysRevB.78.081406>. – DOI 10.1103/PhysRevB.78.081406
- [21] LIPSON, H. ; STOKES, A. R.: The Structure of Graphite. In: *Proceedings of the Royal Society of London A: Mathematical, Physical and Engineering Sciences* 181 (1942), Nr. 984, 101–105. <http://dx.doi.org/10.1098/rspa.1942.0063>. – DOI 10.1098/rspa.1942.0063. – ISSN 0080–4630
- [22] LOUDON, R. : The Raman effect in crystals. In: *Advances in Physics* 13 (1964), Nr. 52, 423–482. <http://dx.doi.org/10.1080/00018736400101051>. – DOI 10.1080/00018736400101051
- [23] MADSEN, G. K. H. ; BLAHA, P. ; SCHWARZ, K. ; SJÖSTEDT, E. ; NORDSTRÖM, L. : Efficient linearization of the augmented plane-wave method. In: *Phys. Rev. B* 64 (2001), Oct, 195134. <http://dx.doi.org/10.1103/PhysRevB.64.195134>. – DOI 10.1103/PhysRevB.64.195134
- [24] MAFRA, D. L. ; SAMSONIDZE, G. ; MALARD, L. M. ; ELIAS, D. C. ; BRANT, J. C. ; PLENTZ, F. ; ALVES, E. S. ; PIMENTA, M. A.: Determination of LA and TO phonon dispersion relations of graphene near the Dirac point by double resonance Raman scattering. In: *Phys. Rev. B* 76 (2007), Dec, 233407. <http://dx.doi.org/10.1103/PhysRevB.76.233407>. – DOI 10.1103/PhysRevB.76.233407
- [25] MAK, K. F. ; JU, L. ; WANG, F. ; HEINZ, T. F.: Optical spectroscopy of graphene: From the far infrared to the ultraviolet. In: *Solid State Communications* 152 (2012), Nr. 15, 1341 - 1349. <http://dx.doi.org/http://dx.doi.org/10.1016/j.ssc.2012.04.064>. – DOI <http://dx.doi.org/10.1016/j.ssc.2012.04.064>. – ISSN 0038–1098. – Exploring Graphene, Recent Research Advances
- [26] MARINOPOULOS, A. G. ; REINING, L. ; RUBIO, A. ; OLEVANO, V. : *Ab initio* study of the optical absorption and wave-vector-dependent dielectric response of graphite. In: *Phys. Rev. B* 69 (2004), Jun, 245419. <http://dx.doi.org/10.1103/PhysRevB.69.245419>. – DOI 10.1103/PhysRevB.69.245419
- [27] NOVOSELOV, K. S. ; GEIM, A. K. ; MOROZOV, S. V. ; JIANG, D. ; ZHANG, Y. ; DUBONOS, S. V. ; GRIGORIEVA, I. V. ; FIRSOV, A. A.: Electric Field Effect in Atomically Thin Carbon Films. In: *Science* 306 (2004), Nr. 5696, 666–669. <http://dx.doi.org/10.1126/science.1102896>. – DOI 10.1126/science.1102896. – ISSN 0036–8075
- [28] ONIDA, G. ; REINING, L. ; RUBIO, A. : Electronic excitations: density-functional versus many-body Green’s-function approaches. In: *Rev. Mod. Phys.* 74 (2002), Jun, 601–659. <http://dx.doi.org/10.1103/RevModPhys.74.601>. – DOI 10.1103/RevModPhys.74.601
- [29] PARK SUNGJIN ; RUOFF RODNEY S.: Chemical methods for the production of graphenes. In: *Nat Nano* 4 (2009), apr, Nr. 4, S.

- 217–224. <http://dx.doi.org/http://dx.doi.org/10.1038/nnano.2009.58>. – DOI <http://dx.doi.org/10.1038/nnano.2009.58>. – ISSN 1748–3387. – 10.1038/nnano.2009.58
- [30] PATON, K. R. ; VARRLA, E. ; BACKES, C. ; SMITH, R. J. ; KHAN, U. ; O’NEILL, A. ; BOLAND, C. ; LOTYA, M. ; ISTRATE, O. M. ; KING, P. ; HIGGINS, T. ; BARWICH, S. ; MAY, P. ; PUCZKARSKI, P. ; AHMED, I. ; MOEBIUS, M. ; PETTERSSON, H. ; LONG, E. ; COELHO, J. ; O’BRIEN, S. E. ; MCGUIRE, E. K. ; SANCHEZ, B. M. ; DUESBERG, G. S. ; MCEVOY, N. ; PENNYCOOK, T. J. ; DOWNING, C. ; CROSSLEY, A. ; NICOLSI, V. ; COLEMAN, J. N.: Scalable production of large quantities of defect-free few-layer graphene by shear exfoliation in liquids. In: *Nat Mater* 13 (2014), Jun, Nr. 6, 624–630. <http://dx.doi.org/10.1038/nmat3944>. – ISSN 1476–1122. – Article
- [31] PERDEW, J. P. ; BURKE, K. ; ERNZERHOF, M. : Generalized Gradient Approximation Made Simple. In: *Phys. Rev. Lett.* 77 (1996), Oct, 3865–3868. <http://dx.doi.org/10.1103/PhysRevLett.77.3865>. – DOI 10.1103/PhysRevLett.77.3865
- [32] PERDEW, J. P. ; WANG, Y. : Accurate and simple analytic representation of the electron-gas correlation energy. In: *Phys. Rev. B* 45 (1992), Jun, 13244–13249. <http://dx.doi.org/10.1103/PhysRevB.45.13244>. – DOI 10.1103/PhysRevB.45.13244
- [33] PETERSILKA, M. ; GOSSMANN, U. J. ; GROSS, E. K. U.: Excitation Energies from Time-Dependent Density-Functional Theory. In: *Phys. Rev. Lett.* 76 (1996), Feb, 1212–1215. <http://dx.doi.org/10.1103/PhysRevLett.76.1212>. – DOI 10.1103/PhysRevLett.76.1212
- [34] PISCANEC, S. ; LAZZERI, M. ; MAURI, F. ; FERRARI, A. C. ; ROBERTSON, J. : Kohn Anomalies and Electron-Phonon Interactions in Graphite. In: *Phys. Rev. Lett.* 93 (2004), Oct, 185503. <http://dx.doi.org/10.1103/PhysRevLett.93.185503>. – DOI 10.1103/PhysRevLett.93.185503
- [35] POPOV, V. N.: Two-phonon Raman bands of bilayer graphene: Revisited. In: *Carbon* 91 (2015), 436 - 444. <http://dx.doi.org/http://dx.doi.org/10.1016/j.carbon.2015.05.020>. – DOI <http://dx.doi.org/10.1016/j.carbon.2015.05.020>. – ISSN 0008–6223
- [36] POPOV, V. N. ; LAMBIN, P. : Theoretical Raman intensity of the G and 2D bands of strained graphene. In: *Carbon* 54 (2013), 86 - 93. <http://dx.doi.org/http://dx.doi.org/10.1016/j.carbon.2012.11.006>. – DOI <http://dx.doi.org/10.1016/j.carbon.2012.11.006>. – ISSN 0008–6223
- [37] RAMAN, C. V.: A new radiation. In: *Indian J. Phys* 2 (1928), S. 387–398
- [38] RANI, P. ; DUBEY, G. S. ; JINDAL, V. : {DFT} study of optical properties of pure and doped graphene. In: *Physica E: Low-dimensional Systems and Nanostructures* 62 (2014), 28 - 35. <http://dx.doi.org/http://dx.doi.org/10.1016/j.physe.2014.04.010>. – DOI <http://dx.doi.org/10.1016/j.physe.2014.04.010>. – ISSN 1386–9477

- [39] REINING, L. ; OLEVANO, V. ; RUBIO, A. ; ONIDA, G. : Excitonic Effects in Solids Described by Time-Dependent Density-Functional Theory. In: *Phys. Rev. Lett.* 88 (2002), Jan, 066404. <http://dx.doi.org/10.1103/PhysRevLett.88.066404>. – DOI 10.1103/PhysRevLett.88.066404
- [40] RIGAMONTI, S. ; BOTTI, S. ; VENIARD, V. ; DRAXL, C. ; REINING, L. ; SOTTILE, F. : Estimating Excitonic Effects in the Absorption Spectra of Solids: Problems and Insight from a Guided Iteration Scheme. In: *Phys. Rev. Lett.* 114 (2015), Apr, 146402. <http://dx.doi.org/10.1103/PhysRevLett.114.146402>. – DOI 10.1103/PhysRevLett.114.146402
- [41] RUNGE, E. ; GROSS, E. K. U.: Density-Functional Theory for Time-Dependent Systems. In: *Phys. Rev. Lett.* 52 (1984), Mar, 997–1000. <http://dx.doi.org/10.1103/PhysRevLett.52.997>. – DOI 10.1103/PhysRevLett.52.997
- [42] SAGMEISTER, S. ; AMBROSCH-DRAXL, C. : Time-dependent density functional theory versus Bethe-Salpeter equation: an all-electron study. In: *Phys. Chem. Chem. Phys.* 11 (2009), 4451-4457. <http://dx.doi.org/10.1039/B903676H>. – DOI 10.1039/B903676H
- [43] SALPETER, E. E. ; BETHE, H. A.: A Relativistic Equation for Bound-State Problems. In: *Phys. Rev.* 84 (1951), Dec, 1232–1242. <http://dx.doi.org/10.1103/PhysRev.84.1232>. – DOI 10.1103/PhysRev.84.1232
- [44] SAVINI, G. ; DAPPE, Y. ; ÖBERG, S. ; CHARLIER, J.-C. ; KATSNELSON, M. ; FASOLINO, A. : Bending modes, elastic constants and mechanical stability of graphitic systems. In: *Carbon* 49 (2011), Nr. 1, 62 - 69. <http://dx.doi.org/http://dx.doi.org/10.1016/j.carbon.2010.08.042>. – DOI <http://dx.doi.org/10.1016/j.carbon.2010.08.042>. – ISSN 0008–6223
- [45] SMEKAL, A. : Zur Quantentheorie der Dispersion. In: *Naturwissenschaften* 11 (1923), Nr. 43, 873–875. <http://dx.doi.org/10.1007/BF01576902>. – DOI 10.1007/BF01576902. – ISSN 1432–1904
- [46] STRINATI, G. : Application of the Green's functions method to the study of the optical properties of semiconductors. In: *La Rivista del Nuovo Cimento (1978-1999)* 11 (1988), Nr. 12, 1–86. <http://dx.doi.org/10.1007/BF02725962>. – DOI 10.1007/BF02725962. – ISSN 1826–9850
- [47] THOMSEN, C. ; REICH, S. : Double Resonant Raman Scattering in Graphite. In: *Phys. Rev. Lett.* 85 (2000), Dec, 5214–5217. <http://dx.doi.org/10.1103/PhysRevLett.85.5214>. – DOI 10.1103/PhysRevLett.85.5214
- [48] TREVISANUTTO, P. E. ; GIORGETTI, C. ; REINING, L. ; LADISA, M. ; OLEVANO, V. : *Ab Initio* GW Many-Body Effects in Graphene. In: *Phys. Rev. Lett.* 101 (2008), Nov, 226405. <http://dx.doi.org/10.1103/PhysRevLett.101.226405>. – DOI 10.1103/PhysRevLett.101.226405
- [49] TREVISANUTTO, P. E. ; HOLZMANN, M. ; CÔTÉ, M. ; OLEVANO, V. : *Ab initio* high-energy excitonic effects in graphite and graphene. In: *Phys. Rev. B* 81 (2010), Mar, 121405. <http://dx.doi.org/10.1103/PhysRevB.81.121405>. – DOI 10.1103/PhysRevB.81.121405

- [50] TRUCANO PETER ; CHEN RUEY: Structure of graphite by neutron diffraction. In: *Nature* 258 (1975), nov, Nr. 5531, S. 136–137. <http://dx.doi.org/http://dx.doi.org/10.1038/258136a0>. – DOI <http://dx.doi.org/10.1038/258136a0>. – 10.1038/258136a0
- [51] VENEZUELA, P. ; LAZZERI, M. ; MAURI, F. : Theory of double-resonant Raman spectra in graphene: Intensity and line shape of defect-induced and two-phonon bands. In: *Phys. Rev. B* 84 (2011), Jul, 035433. <http://dx.doi.org/10.1103/PhysRevB.84.035433>. – DOI 10.1103/PhysRevB.84.035433
- [52] WALLACE, P. R.: The Band Theory of Graphite. In: *Phys. Rev.* 71 (1947), May, 622–634. <http://dx.doi.org/10.1103/PhysRev.71.622>. – DOI 10.1103/PhysRev.71.622
- [53] WANG, M. ; LI, C. M.: Excitonic properties of graphene-based materials. In: *Nanoscale* 4 (2012), 1044-1050. <http://dx.doi.org/10.1039/C1NR10885A>. – DOI 10.1039/C1NR10885A
- [54] YANG, L. ; DESLIPPE, J. ; PARK, C.-H. ; COHEN, M. L. ; LOUIE, S. G.: Excitonic Effects on the Optical Response of Graphene and Bilayer Graphene. In: *Phys. Rev. Lett.* 103 (2009), Oct, 186802. <http://dx.doi.org/10.1103/PhysRevLett.103.186802>. – DOI 10.1103/PhysRevLett.103.186802

Appendix A

Two dimensional materials

As **exciting** is solving the KS equations in reciprocal space, the crystal is always assumed to be periodic in the three directions, defined by the lattice vectors. To simulate isolated two dimensional crystals, a third lattice vector \mathbf{a}_3 is defined orthogonal to the plane spanned by the two lattice vectors \mathbf{a}_1 and \mathbf{a}_2 (see Fig. A.1). This vector has to be long enough to produce a sufficient amount of vacuum between the crystal and its replica, to avoid interactions. For calculations on monolayer graphene, a third lattice vector with length $|\mathbf{a}_3| = 3a$ is used, with the lattice constant a defined in Chapter 1. For bilayer graphene, the interlayer distance is added to \mathbf{a}_3 .

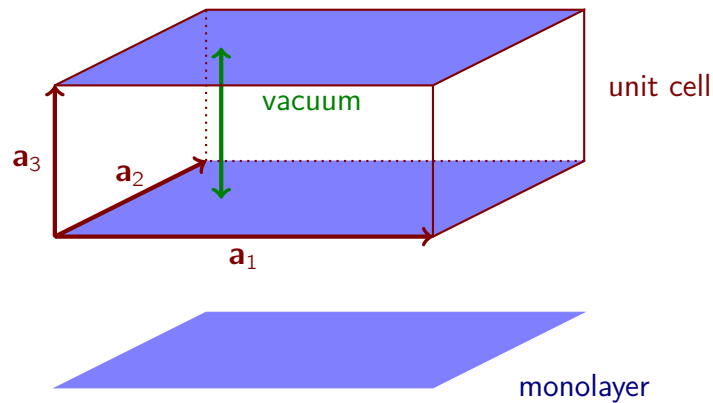


Figure A.1: Unit cell of a two dimensional material.

Appendix B

Convergence with respect to numerical parameters

B.1 Phonons frequencies

In a frozen phonon calculation, the dynamical matrix is calculated from the forces acting on the atoms, calculated in a groundstate calculation. The most important numerical parameter to converge in a groundstate calculation are the basis size, defined by the dimensionless parameter $R_{\text{MT}}G_{\text{max}}$, and the \mathbf{k} -grid for sampling the Brillouin zone. The frequencies of the Raman active optical in-plane Γ point modes for different values of $R_{\text{MT}}G_{\text{max}}$ and \mathbf{k} -grids are given in Tab. B.1. With $R_{\text{MT}}G_{\text{max}} = 7$ and a \mathbf{k} -grid of 32×32 , an accuracy of less than 1 cm^{-1} is reached.

$R_{\text{MT}}G_{\text{max}} \backslash \mathbf{k}$ -grid	4	5	6	7	8
16x16			1563.6		
20x20	1602.9	1542.7	1561.5	1562.1	1562.1
25x25				1559.2	
32x32				1557.4	
40x40				1557.3	

Table B.1: PBE optical in-plane Γ point phonon frequency in cm^{-1} for different numerical parameters. Converged values are expected in the bottom right corner with high values of $R_{\text{MT}}G_{\text{max}}$, which defines the basis size, and a dense \mathbf{k} -grid for sampling the Brillouin zone.

For a good phonon dispersion, on the other hand also the phonon calculations have to be converged with respect to the \mathbf{q} -grid for interpolating the dynamical matrix over the Brillouin zone. In a practical calculation, one often has to choose which parameters are more important to converge. In this thesis, phonon dispersions were calculated with parameters $R_{\text{MT}}G_{\text{max}} = 6$, a \mathbf{k} -grid of 16×16 and a \mathbf{q} -grid of 6×6 for LDA and 12×12 for PBE calculations.

List of abbreviations

Acronym	Designation
APW	Augmented plane waves
BSE	Bethe-Salpeter equation
BZ	Brillouin zone
DOS	Density of states
DFT	Density-functional theory
GGA	Generalized gradient approximation
IP	Independent particle
<i>I</i>	Interstitial region
KS	Kohn-Sham
LAPW	Linearized augmented plane waves
LDA	Local-density approximation
lo	Local orbital
MT	Muffin-tin
RPA	Random-phase approximation
TDDFT	Time-dependent density-functional theory

List of symbols

Symbol	Designation
V_E	Unit cell volume
V_S	Scattering volume
ε_M	Macroscopic dielectric function
S	Raman-scattering efficiency
α	Atomic index
l	Lattice index
k	Cartesian index
μ	Combined index
Q	Complex phonon normal coordinate
\bar{Q}	Real phonon normal coordinate
ω	Phonon or photon frequency
w	Phonon eigenvector
u	Atomic displacements
\mathbf{R}	Lattice vector
\mathbf{k}, \mathbf{q}	Reciprocal vector in first BZ
\mathbf{G}	Reciprocal lattice vector
Ψ	Full wave function
ψ	Electronic wave function
χ	Nuclear wave function
φ	KS wave function
Φ	Interatomic force constants
N_{at}	Number of atoms in unit cell
N_{cell}	Number of unit cells in phonon coherence volume
N_{SC}	Number of unit cells in supercell
n	Electron density

Acknowledgement

I want to acknowledge the extraordinary supervision and continuous support in all situations of my supervisor Claudia Draxl, leader of the solid-state theory group at Humboldt-Universität Berlin. A special thank goes to my mentors Caterina Cocchi and Pasquale Pavone who supported me throughout my thesis. With their great knowledge and experience, they helped me whenever I had questions about my research or writing, or ran into problems. I want to extend my gratitude to all members of the solid-state theory group at Humboldt-Universität Berlin for insightful discussions.

Selbständigkeitserklärung

Hiermit erkläre ich, dass ich die vorliegende Arbeit selbstständig verfasst und keine anderen als die angegebenen Quellen und Hilfsmittel benutzt habe.

Berlin, den 25. Juli 2016

(Unterschrift)